Mon. Not. R. Astron. Soc. **311**, 762–780 (2000)

Testing linear-theory predictions of galaxy formation

Ben Sugerman,[1,2★] F. J. Summers[2,3★] and Marc Kamionkowski[2,4★]

[1]*Department of Astronomy, Columbia University, 538 West 120th Street, New York, NY 10027, USA*
[2]*Columbia Astrophysics Lab, Columbia University, 538 West 120th Street, New York, NY 10027, USA*
[3]*Department of Astrophysics, American Museum of Natural History, Central Park West at 79th Street, New York, NY 10024, USA*
[4]*Department of Physics, Columbia University, 538 West 120th Street, New York, NY 10027, USA*

Accepted 1999 September 10. Received 1999 July 30; in original form 1998 December 15

ABSTRACT

The angular momentum of galaxies is routinely ascribed to a process of tidal torques acting during the early stages of gravitational collapse, and is predicted from the initial mass distribution using second-order perturbation theory and the Zel'dovich approximation. We test this theory for a flat hierarchical cosmogony using a large *N*-body simulation with sufficient dynamic range to include tidal fields, allow resolution of individual galaxies, and thereby expand on previous studies. The predictions of linear collapse, linear tidal torque, and biased-peaks galaxy formation are applied to the initial conditions and compared with results for evolved bound objects. We find relatively good correlation between the predictions of linear theory and actual galaxy evolution. Collapse is well described by an ellipsoidal model within a shear field, which results primarily in triaxial objects that do not map directly to the initial density field. While structure formation from early times is a complex history of hierarchical merging, salient features are well described by the simple spherical-collapse model. Most notably, we test several methods for determining the turnaround epoch, and find that turnaround is successfully described by the spherical-collapse model. The angular momentum of collapsing structures grows linearly until turnaround, as predicted, and continues quasi-linearly until shell crossing. The predicted angular momentum for well-resolved galaxies at turnaround overestimates the true turnaround and final values by a factor of $\sim$3, with a scatter of $\sim$70 per cent, and only marginally yields the correct direction of the angular momentum vector. We recover the prediction that final angular momentum scales as mass to the 5/3 power. We find that mass and angular momentum also vary proportionally with peak height. In view of the fact that the observed galaxy collapse is a stochastic hierarchical and non-linear process, it is encouraging that the linear theory can serve as an effective predictive and analytic tool.

Key words: methods: numerical – galaxies: formation – cosmology: theory – dark matter – large-scale structure of Universe.

1 INTRODUCTION

Large-scale-structure formation (i.e., galaxies and clusters) most likely resulted from gravitational amplification of small density inhomogeneities in an otherwise smooth primordial density field following an initial hot big bang. This scenario is supported by the *COBE* findings of the cosmic microwave background radiation anisotropies (Smoot et al. 1992). In the standard-CDM (cold dark matter) model (Peebles 1982; Bond & Szalay 1983; Bond & Efstathiou 1984), these fluctuations grow in the non-baryonic dark matter (DM) component before recombination, thereby providing the density perturbations which evolve into structures and voids (for reviews, see Ostriker 1993 and Peebles 1993). The evolution of these inhomogeneities are relatively easily studied using linear perturbation theory as long as the density contrast is small compared to unity, i.e., within the linear regime. However, once the density contrast exceeds unity, linear theory breaks down and either analytic approximations or *N*-body simulations must be invoked to study the evolution of perturbations.

Application of perturbation approximations in the linear regime may offer insight into a protogalaxy's acquisition of angular momentum during separation and collapse from the Hubble flow. Hoyle (1949, cf. Sciama 1955) first suggested that a protogalaxy's spin arises from the tidal fields of its neighbours. An alternative theory, in which galactic spin is the relic of primeval vorticity, is

★ E-mail: ben@astro.columbia.edu (BS); summers@amnh.org (FJS); kamion@phys.columbia.edu (MK)

© 2000 RAS

Downloaded from https://academic.oup.com/mnras/article-abstract/311/4/762/1746627 by California Institute of Technology user on 19 May 2020

not widely regarded as favourable (see the review by Efstathiou & Silk 1983). Peebles (1969) first examined Hoyle's theory using a second-order perturbative expansion to find the growth rate of angular momentum induced by gravitational tidal torques from the surrounding expanding matter field. In particular, he found that the angular momentum within a spherical comoving volume grows as $t^{5/3}$ in an Einstein–de Sitter universe. Second-order expansion is necessary, since to first order, an isotropic spherical volume can not gain angular momentum from external torques. Doroshkevich (1970) found that for a generic non-spherical volume enclosing a protogalaxy, the angular-momentum growth rate at early times (in a flat cosmology) is linearly proportional to time, and that Peebles' growth rate resulted from incorrect symmetries. White (1984) determined that Peebles' findings resulted from surface effects which convect angular momentum across the boundary of the enclosing Eulerian volume, and correctly reinterpreted the analysis to yield the predicted linear growth rate. White noted that his approximations strictly apply only to early times, during which the density contrast (or the density field convolved with a window function of protogalactic scale) is much less than unity, and that the final spin is dependent entirely on how the tidal torquing is terminated. Following the collapse history dictated by the spherical-collapse model (Partridge & Peebles 1967; Gunn & Gott 1972; Peebles 1980, chapter 19), one typically assumes that a galaxy becomes insensitive to the external tidal field once it separates from the Hubble flow and begins collapse (Peebles 1969).

Peebles' and White's analyses involve volumes centred on random points; hence the matter contained within those volumes is not guaranteed to collapse into a bound protogalaxy. However, we expect that protogalaxies will form in regions of density peaks, currently known as the biased galaxy-formation model (e.g. Kaiser 1984; Peacock & Heavens 1985; Bardeen et al. 1986). A revised model has been proposed, in which second-order perturbation expansions describe tidal torques from high-density peaks acting on the primordial mass distribution of a protogalaxy, and has been analysed by, e.g., Hoffman (1986, 1988) and Catelan & Theuns (1996a, hereafter CT96). The acquisition of angular momentum from tidal fields and the role of tidal shear have also been studied by, e.g., Binney & Silk (1979), Heavens & Peacock (1988, hereafter HP88), Ryden (1988), Dubinski (1992), Quinn & Binney (1992), Bond & Myers (1993), Zaroubi & Hoffman (1993), Bertschinger & Jain (1994), van de Weygaert & Babul (1994) and Eisenstein & Loeb (1995, hereafter EL95).

Early quantitative comparison of angular-momentum evolution with linear theory was first addressed by Peebles (1971) and Efstathiou & Jones (1979). White (1984), using two 32 768-particle *N*-body simulations, found that the *mean* angular momentum over all groups grows linearly at very early times ($a \lesssim 2$); however, from the individual examples he shows, one is led to conclude that the dispersion about this value is quite high. Barnes & Efstathiou (1987, hereafter BE87) also draw the same conclusion from seven simulations using 8000–32 768 particles and a variety of initial conditions. Again, the mean growth of L at early times appears linear, while the individual galaxies exhibit a significant dispersion. BE87 further concluded that the linear prediction for the final angular momentum provides only an order-of-magnitude estimate.

In this paper we address the predictions of linear theory and test their validity using a P3MSPH gravitational and hydrodynamic simulation. We expand on previous numerical studies by using galaxies evolved with higher numerical and spatial resolution. Following the collapse history and evolution of 77 galaxies from high redshift until the present epoch, we compare the angular momentum to linear theory, to study the accuracy and limits of applicability of this formalism. We address whether the linear-theory approximation is applicable in the weakly non-linear and strictly non-linear regimes. We examine the role and significance of local effects such as mergers and close tidal encounters on the evolutionary history. We further examine various models of protogalactic collapse and comment on the applicability and limitations of each. In a hierarchical-clustering cosmogony, structure formation is not expected to follow a simple spherical-collapse model. Therefore it is most advantageous if the linear theory successfully predicts the final angular momentum of a collapsing protogalaxy, for use as a computational tool, numerical shortcut, and in reconstructing the primordial density field.

The layout of the paper is as follows. In Section 2 we briefly review White's formalism for linear tidal torques, as well as the predictions of the spherical-collapse model. We describe the numerical simulation, group-finding, and our galaxy catalogue in Section 3, and our methodology for measuring pertinent parameters for each galaxy in Section 4. Results are presented in Section 5. We first examine the collapse history of galaxies and compare the qualitative and quantitative predictions of linear theory to the evolution of our set of galaxies. We then discuss scalings derived from linear theory, compare predictions of the biased galaxy-formation scenario to our data, and briefly discuss correlations. The paper concludes with a discussion in Section 6.

2 DYNAMICAL FORMALISM

For completeness, we present the derivation of the linear theory developed by White (1984) using the Zel'dovich (1970) approximation. Consider the matter within an expanding Friedmann universe to be adequately described as a Newtonian pressureless cold fluid. The linear-theory mapping between the Eulerian and Lagrangian comoving coordinates $\boldsymbol{x}$ and $\boldsymbol{q}$ (respectively) is given by

$$\boldsymbol{x}(\boldsymbol{q}, t) = \boldsymbol{q} - D(t)\nabla\psi(\boldsymbol{q}), \tag{1}$$

where $\boldsymbol{q}$ is defined as the $\boldsymbol{x}$ position of a particle as $t \rightarrow 0$, and $\nabla\psi$ is proportional to the peculiar gravitational potential. $D(t)$ describes the growing density mode. Equation (1) is a statement of the Zel'dovich approximation, and is strictly valid only if $\langle\delta\rangle \ll 1$, where the fractional density contrast $\delta(\boldsymbol{r}, t) = \rho(\boldsymbol{r}, t)/\rho_{\rm b}(t) - 1$. This condition is satisfied if the initial density fluctuations have coherence lengths of protogalactic size. However, since this may be the case only at the earliest times, we smooth the density field by convolving it with a window function of protogalactic scale. This implicitly assumes that small-scale non-linearities have negligible effect on large-scale fluctuations at early times (White 1984).

The angular momentum of the matter contained within an Eulerian volume V, neglecting centre of mass motion, is given by

$$\boldsymbol{L}(t) = \int_{a^3V} {\rm d}\boldsymbol{r}\rho\boldsymbol{r}\times\dot{\boldsymbol{r}} = \rho_{\rm b}a^5\int_V {\rm d}\boldsymbol{x}(1+\delta)\boldsymbol{x}\times\boldsymbol{u}, \tag{2}$$

where $\boldsymbol{u} = \dot{\boldsymbol{x}}$, a dot refers to the normal time derivative, $\boldsymbol{r} = a(t)\boldsymbol{x}$, and a is the cosmological expansion factor. If the transformation tensor $\boldsymbol{T}$ between Eulerian and Lagrangian coordinates is defined such that $\boldsymbol{x}(\boldsymbol{q}, t) = \boldsymbol{T}\boldsymbol{q}$, then the Jacobian J of $\boldsymbol{T}$ is the change in volume between Eulerian and Lagrangian coordinates. Since

Downloaded from https://academic.oup.com/mnras/article-abstract/311/4/762/1746627 by California Institute of Technology user on 19 May 2020

Eulerian and Lagrangian coordinates are identical at $t = 0$, $J(t = 0) \equiv 1$, it follows directly that $\rho/\rho_0 = J(0)/J(t)$. If $\rho_b = \rho_0$, i.e., the background mean density is equal to the primordial density, then we immediately retrieve the continuity equation,

$$1 + \delta[\boldsymbol{x}(\boldsymbol{q}, t), t] = J^{-1}. \tag{3}$$

From equation (1), we find the peculiar velocity,

$$\boldsymbol{v}(\boldsymbol{q}, t) = a\boldsymbol{u}(\boldsymbol{q}, t) = a\dot{D}\nabla\psi. \tag{4}$$

We now transform the integral (2) to the Lagrangian volume Γ,

$$\boldsymbol{L}(t) = \eta_0 a^2 \dot{D} \int_\Gamma \mathrm{d}\boldsymbol{q}\, \boldsymbol{q} \times \nabla\psi(\boldsymbol{q}), \tag{5}$$

where $\eta_0 \equiv \rho_b a^3 = \rho_0 a_0^3$. It is obvious from equation (5) that the angular momentum $\boldsymbol{L}$ depends on the shape of the volume Γ that encloses the constituents of the protogalaxy. Following White (1984), we approximate the potential ψ by the first three terms of the Taylor series about the origin $\boldsymbol{q} = 0$. The linear approximation for the angular momentum may then be expressed as

$$L_i^{(1)}(t) = a(t)^2 \dot{D}(t) \epsilon_{ijk} \mathcal{D}_{jl}^{(1)} \mathcal{I}_{lk}, \tag{6}$$

where

$$\mathcal{D}_{ij}^{(1)} = \partial_i \partial_j \psi(0) \tag{7}$$

is the initial deformation tensor at the origin $\boldsymbol{q} = \boldsymbol{0}$,

$$\mathcal{I}_{ij} = \eta_0 \int_\Gamma q_i q_j \, \mathrm{d}\boldsymbol{q} \tag{8}$$

is the inertia tensor, ϵ_{ijk} is the antisymmetric Levi–Civita tensor, and summation over repeated indices is implicit. Since the principal axes of the deformation and inertia tensors are, in general, not aligned for a non-spherical volume, this linear angular momentum should be non-zero.

The time dependence in $L^{(1)}$ lies in the term $a^2(t)\dot{D}(t)$, which for an Einstein–de Sitter universe equals $\frac{2}{3}t/t_o^2$ such that $L^{(1)}$ grows linearly in time. One simplifies the computation of the deformation tensor using the Fourier transform of the potential $\tilde{\psi}(\boldsymbol{k})$, where $\boldsymbol{k}$ is the comoving Lagrangian wavevector. The deformation tensor is now

$$\mathcal{D}_{ij}^{(1)} = -\int \frac{\mathrm{d}\boldsymbol{k}}{(2\pi)^3} k_i k_j \tilde{\psi}(\boldsymbol{k}) \tilde{W}(k, R), \tag{9}$$

and $\tilde{W}(k, R)$ is the Fourier transform of the smoothing function $W_R(\boldsymbol{q})$. By filtering ψ on scale R, we effectively filter out non-linear mode coupling, thereby restricting our approximations to linear evolution only.

One expects that the angular momentum of a galaxy will grow only as long as the particle distribution is sensitive to large-scale tidal couplings (Peebles 1969, 1980). When the density contrast is small, the gravitational field of a protogalaxy acts to collapse the object, while the rotation induced by the tidal field of the surrounding matter opposes this contraction. Under the assumption of spherical evolution, the tidal influence of surrounding matter is important until the density contrast $\delta \sim 1$, at which point one can consider the protogalaxy as an isolated collapsing system (Peebles 1980).

To model its early evolution, we treat the protogalaxy as a spherical overdense region in an otherwise flat universe (Partridge & Peebles 1967; Gunn & Gott 1972; Peebles 1980, chapter 19), and evolve the particles according to the closed Friedmann equations (the spherical-collapse model). Specifically, inside the overdense region, $\rho(r) = \rho > \bar{\rho}$, whereas outside, $\rho(r) = \bar{\rho}$ and $\bar{\rho}$ is defined by the flat Friedmann model. In this formalism, the galaxy should decouple from the tidal field at the turnaround epoch t_M, defined as the time of maximum expansion and characterized in this model by an overdensity $\delta \simeq 4.55$. Virialization of the protogalaxy occurs when the inner mass shells pass through the centre, at which point time-varying gravitational fields dissipate energy and relax the system. This dissipation process is known as violent relaxation, and we refer to these shell crossings through centre as caustic crossings. In the approximation that we treat a non-spherical, non-uniform distribution undergoing hierarchical collapse as a smoothly evolving closed universe, we can also predict (to first order) the time of caustic crossing from the Friedmann equations as $t_C \simeq 2t_M$.

Had the region not collapsed but expanded linearly, turnaround would occur when the overdensity (Peebles 1980)

$$\delta = \frac{3}{20}(6\pi)^{2/3}. \tag{10}$$

Since turnaround occurs in the weakly non-linear regime, we must apply $L^{(1)}$ beyond its region of strict validity. It is therefore of interest to study how far into the non-linear regime, if even as far as turnaround, one may successfully apply the linear prediction. Furthermore, the Jacobian transformation J^{-1} is non-vanishing up until caustic crossing (Shandarin & Zel'dovich 1989). Therefore we expect that $L^{(1)}$ will be valid at most until caustic crossing.

3 NUMERICAL SIMULATION AND GALAXY CATALOGUE

3.1 Numerical simulation

To test the linear-theory approximation (equation 6), we have performed a high-resolution galaxy-formation simulation using the P3MSPH code (Evrard 1988; Summers 1993), which incorporates large- and short-scale gravitational forces with smooth-particle hydrodynamics (Hockney & Eastwood 1981; Monaghan 1992). We chose a $16\,h^{-1}$ Mpc comoving box length with periodic boundary conditions in a standard-CDM Einstein–de Sitter universe ($\Omega = 1$, $\Omega_b = 0.05$, $H_0 = 100\,h\,\mathrm{km\,s^{-1}\,Mpc^{-1}}$, and $h = 0.5$). Initial conditions were generated using a so-called 'glass' initial distribution (White 1994) and the Zel'dovich approximation.

To follow galaxy-scale evolution while including larger scale tidal fields within a reasonable computational time, our simulation utilizes multiple resolution regions. A simulation with 128^3 gas and 128^3 DM particles was evolved until initial structures had formed. Using the results of this partially evolved simulation, we chose a cubic subregion $8\,h^{-1}$ Mpc on a side for study. The subregion was chosen to contain a mixture of density regions, yet avoid the centre of a rich cluster. The 258 530 gas and 258 530 dark-matter particles in this subregion were retained at high resolution. The remaining particles outside this subregion were combined and collapsed into 229 933 'super' dark matter (SDM) particles (e.g. Katz & White 1993). The gas:DM:SDM mass ratio is 1:19:160, with a DM mass of roughly $10^9\,\mathrm{M}_\odot$ and a total simulation mass of $2.27 \times 10^{15}\,\mathrm{M}_\odot$.

The gravitational softening length for a Plummer-law force was set to 8 kpc (comoving), with the SPH smoothing length limited to a minimum of one-third the gravitational softening. The parameters

Downloaded from https://academic.oup.com/mnras/article-abstract/311/4/762/1746627 by California Institute of Technology user on 19 May 2020

are appropriate to provide enough resolution for the formation and evolution of galaxies (see the note in Section 5 regarding the use of gas particles within this region). The simulation is evolved from the initial epoch at $z = 32$ ($t_i = 68.8$ Myr) to $z = 0$ ($t_f = 13.04$ Gyr) using 5000 time-steps of 2.592 Myr. Outputs are generated every 25 steps during the initial evolution (10 per cent) and every 100 steps thereafter.

3.2 Group-finding algorithm

It should be clearly noted that numerical simulations of this sort do not form 'galaxies,' *per se*. However, we can identify the sites of most probable galaxy formation as regions of the highest overdensity, containing 'haloes' of DM particles inside of whose potential wells reside dense gaseous components. In gravitational simulations of this nature, discrete boundaries between the virialized galaxies and the outer unbound particles do not exist, therefore the group-finding method must rely on an arbitrary criterion, such as local overdensity or interparticle spacing. The problem of group-finding is therefore non-trivial, and has been thoroughly examined by, e.g., Summers, Davis & Evrard (1995) and Eisenstein & Hut (1998). Ideally, we would prefer to identify a galaxy as *all* the particles in the simulation which are gravitationally bound as one structure. However, as this is an N^2 calculation, it is computationally far too expensive for practical use. We chose instead to define a group as a collection of $N_{\rm min}$ or more particles all separated by less than a specified linking length η, known as the 'friends-of-friends' (FOF) approach. Groups found with this method generally lie within a minimum overdensity contour given by

$$\delta_{\rm min} = \frac{2\Omega}{(4/3)\pi\eta^3}. \tag{11}$$

Since this is only a minimum contour level, the actual average overdensity of a galaxy will be many times larger. The FOF algorithm considers only interparticle spacing as the criteria for forming a group, and thereby does not distinguish between particles which are gravitationally bound to the system. As a first-order solution, once a list is generated of all particles forming a group according to the FOF routine, we recursively compute the local potential of that ensemble and remove any unbound particles.

To identify a galaxy, we generate two independent catalogues of gas and DM groups found using FOF at the final output ($z = 0$). Gas groups must contain at least 25 bound particles and DM groups at least 100, both using a linking length, in units of the mean interparticle spacing, of $\eta = 0.075$, which corresponds to a minimum overdensity contour $\delta_{\rm min} \sim 1000$. We then cross-correlate the positions of the most-bound particle in each group, throwing out any group which does not have a corresponding counterpart in the other species, and create a catalogue of galaxies containing both bound DM and gas components. With this method, we have identified 98 galaxies within the simulation. Other galaxies exist within cluster regions of the simulation, but, if the dark-matter halo is mixed within the general cluster halo, the galaxy is unsuitable for our analysis.

3.3 Selection criteria and galaxy catalogue

Once the catalogue is made, the particles within any galaxy may be traced back to any epoch, since every particle in the simulation is labelled with an ID number, which it maintains throughout the entire run. Groups whose initial distributions were too close to the subregion boundary must be excluded from the catalogue. Not only do these have artificially distorted primordial distributions, but since they are located at the boundary with the SDM region, these border groups contain an unreasonably large number of SDM particles, which introduce extraordinary gravitational perturbations to the evolving galaxy. Therefore we also disregard any galaxies containing a significant number ($N_{\rm SDM} \gtrsim 0.1 N_{\rm DM}$) of SDM particles.

Galaxies which have undergone large merger events or are still merging at the final output are tagged as questionable with respect to the angular-momentum analysis. Angular momentum is not in a stable state during merging and gravitational relaxation. Furthermore, in a large merger, particles within the constituent clumps at earlier times may flow out of the system and hence not be included in the particle list created at the final output. This can cause (as we shall see) a significant amount of angular momentum to flow into or out of the system at any time, and radically distort the measured evolution.[1]

Of the 98 galaxies in our catalogue, 12 are discarded for violating boundary conditions, three are discarded and 10 are tagged as questionable due to mergers, and six are discarded for containing too many SDM particles (all 'questionable' galaxies remain in the catalogue). This leaves a usable catalogue of 77 galaxies.

4 GALAXY PARAMETERS

For each of the galaxies identified in our catalogue, we measure a variety of characteristics for analysis, outlined in the following subsections.

4.1 Lagrangian versus Eulerian descriptions

One can utilize either a Lagrangian or Eulerian description in the analysis of a galaxy. The Lagrangian description Γ is, for our purposes, defined to be the list of particles which constitute a given galaxy. Γ conserves particle number (i.e., mass) for all time, and does not allow for flux of particles into or out of the system. The Eulerian description of a galaxy is taken to be the list of particles lying within the best-fitting ellipsoidal volume V (described in the next subsection) enclosing the Lagrangian list Γ. V can be made to conserve mass if one requires that the volume encloses the same number of particles as Γ; as a galaxy evolves and deforms, V will vary significantly over time.

4.2 Principal axes and ellipsoidal fits

The volume V of a galaxy is determined from its ellipsoidal parameters. However, the accurate determination of axial ratios or orientation angles of a discrete distribution of particles is far from trivial. Many groups (e.g. Plionis, Barrow & Frenk 1991; de Theije, Katgert & van Kampen 1995; Splinter et al. 1997) use the fact that, for a uniform ellipsoid, the ratio of the eigenvalues of the (normalized) inertia tensor is the square of the ratio of the axes. One can then simply fit spherical shells to haloes

[1] This may introduce a bias against non-linear effects, as noted by the referee. In this paper we study the predictive capacity of linear theory in environments which should be the most stable, and we will present a full examination of evolutionary histories in Paper II. However, of the 13 merging galaxies in the catalogue, we discard only three.

Downloaded from https://academic.oup.com/mnras/article-abstract/311/4/762/1746627 by California Institute of Technology user on 19 May 2020

and determine the axis ratios from the normalized inertia tensor, as in Frenk et al. (1988). This method systematically underestimates the axis ratios for non-spherical distributions. Katz (1991) computes the axis ratios from the diagonalized inertia tensor by iteratively deforming an initial spherical shell into an ellipsoid. The axis ratios in each step are determined from the particles contained within the ellipsoid of the previous step, but the major axis is held at a fixed value for all steps. Dubinski & Carlberg (1991) (the DC method) iteratively perform a similar analysis in which the normalization parameter for the inertia tensor, and the axis ratios are recursively determined from each other. Of all these methods, the last is the most aesthetically appealing, since it relies on the smallest number of assumptions (namely, only that the density distribution is stratified in similar ellipsoids). In test scenarios using a $\rho \propto r^{-2}$ density profile, DC find random errors between 1 and 10 per cent, and note that there is a bias toward underestimating the axis ratios if the intrinsic values are $\gtrsim$0.8.

To avoid appealing to initially spherical symmetries, we perform shape analyses on the full bound-particle list Γ for each galaxy. We determine the principal axes and Euler angles (used to rotate between the body and Cartesian coordinate systems) by finding the eigenvectors of the full three-dimensional inertia tensor,

$$I_{ij} = \sum_{\alpha=1}^{M(\Gamma)} m_\alpha \left[\delta_{ij} \sum_k x_k^2 - x_i^\alpha x_j^\alpha \right]. \tag{12}$$

Axes vectors $(\boldsymbol{a}, \boldsymbol{b}, \boldsymbol{c})$ are assigned such that $a \geq b \geq c$, and the Euler angles such that the body $\boldsymbol{a}$ axis is rotated on to the Cartesian $\boldsymbol{x}$ axis. Once the galaxy is translated and rotated on to the Cartesian basis, the axis ratios are determined using the eigenvalues ($e = \sqrt{\lambda_2/\lambda_1}$) of the the two-dimensional inertia tensors for the particles projected on to the $x-y$ and $x-z$ planes (effectively equivalent to the non-iterative method of Katz 1991). One has the option to iterate between the rotation and projected axis ratios until a desired residual is achieved. The best-fitting volume V is now defined to be the ellipsoid using these axis ratios and which contains the same mass as in the Lagrangian volume Γ.

We compared this method to the DC method for test galaxies with random orientations and axis ratios, containing between $N = 100$ and 10 000 particles and following density profiles $\rho \propto r^\eta$ for $\eta \in [0, -3]$. For each combination of particle number and density power law, we ran one test with 1000 galaxies having random axis ratios $\geq$0.1, and a second test with 500 spheroidal galaxies having axis ratios $\geq$0.8. A subsample of the results are listed in Table 1, which shows the average error in the computed axis ratios and χ^2 (the sum of the squares of the per cent errors for all the fits). In roughly every case except $\eta = -3$ (for which both methods fail), our fitting routine achieves at least twice the accuracy of the DC method, with a substantially lower scatter about the mean. We find that for the spheroidal galaxies, there is a slightly higher tendency for both methods to underestimate (by $\lesssim$10 per cent) the actual axial ratios. We note that this technique does not resolve radial structure, as in Warren et al. (1992). However, this is also not our goal, given that the majority of our galaxies contain less than 1000 particles per species.

Table 1. Statistics for elliptical axis fitting.

Axis Ratio	N	η	DC Method $\langle$ % error $\rangle$	DC Method χ^2	Our Method $\langle$ % error $\rangle$	Our Method χ^2
$\geq$0.1	250	0	11. ± 30.	206.	4.4 ± 3.5	6.3
		−2	11. ± 21.	114.	5.3 ± 4.3	9.2
	1000	0	8.2 ± 26.	148.	2.2 ± 2.2	1.9
		−2	8.5 ± 25.	143.	2.8 ± 2.4	2.7
	5000	0	4.6 ± 17.	64.	1.1 ± 1.8	0.88
		−2	5.2 ± 19.	75.	1.4 ± 1.7	0.97
$\geq$0.8	250	0	7.5 ± 5.4	8.6	4.6 ± 3.3	3.2
		−2	7.1 ± 5.7	8.2	5.6 ± 3.9	4.7
	1000	0	3.7 ± 2.8	2.2	2.2 ± 1.6	0.76
		−2	3.8 ± 2.9	2.3	2.6 ± 2.0	1.1
	5000	0	1.8 ± 1.9	0.68	0.96 ± 0.75	0.15
		−2	2.2 ± 2.4	1.1	1.1 ± 0.90	0.22

4.3 Overdensity

For any given galaxy n and epoch t, the overdensity $\delta^{(n)}(t)$ is calculated using the density $\rho^{(n)}(t)$ as given by the best-fitting ellipsoidal volume V and the total mass of particles within that volume. At the earliest times, the overdensities are extremely small and the calculation is not strictly robust, mostly since identification of the volume exactly enclosing a stochastic distribution is non-trivial. At the initial epoch, we also calculate the initial overdensity threshold parameter ν, defined such that $\delta_{\rm i}(M) = \nu\sigma(M)$, where $\sigma(M)$ is the standard deviation of the overdensity as measured on the mass-scale of the galaxy in question. For each galaxy of mass M, we determine $\sigma(M)$ by sampling the overdensity of 10 000 randomly placed spheres, each also containing M particles. This differs from BE87, as Hoffman (1988) has pointed out that their method may introduce bias in ν by calculating σ on a physical smoothing scale rather than a galaxy's mass-scale.

4.4 Predicted and actual angular momentum

We compute $\boldsymbol{L}(t)$ directly for each galaxy from its Lagrangian particle list Γ (containing M particles) using

$$\boldsymbol{L} = \sum_{\alpha=1}^{M} (\boldsymbol{r}_\alpha \times m_\alpha \boldsymbol{v}_\alpha). \tag{13}$$

We calculate the predicted angular momentum from equation (6) by computing the deformation tensor $\mathcal{D}$ and inertia tensor $\mathcal{I}$ for each galaxy at the initial epoch *only*, and evolve their tensor product forward using the time-dependent factor $a^2\dot{D}$. The deformation tensor, as given by equation (9), requires the Fourier transform of the potential $\tilde{\psi}(\boldsymbol{k})$. The entire mass distribution is first smoothed on to a uniform grid using the three-dimensional S2 window function (Hockney & Eastwood 1981),

$$W(r,a) = \begin{cases} \dfrac{48}{\pi a^4}\left(\dfrac{a}{2} - r\right), & \text{if } r < \dfrac{a}{2}, \\ 0, & \text{otherwise.} \end{cases} \tag{14}$$

Note that our S2 smoothing function utilizes the full 3D smoothing of a spherical volume on to a grid, as opposed to using three 1D smoothings as is done, for example, in the triangular-shaped clouds method.

The resulting density field is Fourier transformed and convolved with a Green's function to yield the k-space potential, which is evaluated in equation (9) along with the Fourier transform of the S2 function

$$\tilde{W}(k,a) = \frac{12}{(ka/2)^4}\left(2 - 2\cos\frac{ka}{2} - \frac{ka}{2}\sin\frac{ka}{2}\right). \tag{15}$$

Downloaded from https://academic.oup.com/mnras/article-abstract/311/4/762/1746627 by California Institute of Technology user on 19 May 2020

Values for L and $L^{(1)}$ will be given in the unconventional units of $10^{12}\,\mathrm{M}_{\odot}\,\mathrm{kpc}^2\,\mathrm{Gyr}^{-1}$.

4.5 Turnaround and crossing times

Determination of the turnaround time is another non-trivial problem. Indeed, it is unclear whether an evolving protogalaxy ever passes through a period of maximal isotropic expansion, or whether all material at a given distance from the centre undergoes turnaround at a common time (Peebles 1980, p. 86). Any prediction (e.g., the final angular momentum) that is based upon an ill-defined dynamical point during evolution (e.g., the angular momentum at turnaround) will necessarily be skewed by the uncertainty in determining that epoch. It is therefore important to understand both the uncertainty involved in localizing the turnaround epoch and how this propagates through linear predictions.

To explore statistical consistency, we define four independent methods to determine the turnaround time for each galaxy: the first two empirical, the third semi-empirical, and the last analytic. In the first method, we calculate the average radial velocity of particles with respect to the galaxy's centre of mass. Turnaround t_{Md} is defined as the time when this velocity divergence inverts from positive (expansion) to negative (contraction). The second method defines turnaround $t_{M\%}$ as the earliest time at which at least half the particles in a galaxy are infalling. The semi-empirical method measures the overdensity of the galaxy at each epoch and defines the turnaround $t_{M\delta}$ as the time at which $\delta(t) \simeq 4.55$ (from the spherical-collapse model, Section 2). The analytic method measures the initial overdensity of each galaxy and calculates the epoch t_{Mz} from equation (10) such that

$$z_M = [(20/3)\delta_{\mathrm{i}}(1+z_{\mathrm{i}})(6\pi)^{-2/3}] - 1, \qquad (16)$$

where subscript i indicates the initial value.

Similarly, we use four methods to determine the time of caustic crossing. As explained above, our first-order definition is $t_{Cto} = 2\langle t_M \rangle$. Once virialized, the galaxy will have shrunk by a factor of 2, thereby increasing its density eight-fold, and we expect (again to first order) that $\delta_C \simeq 8\delta_M = 43$ at $t_{C\delta}$. When computing the velocity divergence, we also calculate the variance in the peculiar velocities of all particles in a galaxy, and we expect that this value will be highest (i.e., the most disorder in the velocity field) when the galaxy experiences shell crossing ($t_{C\sigma}$). Finally, if an ellipsoidal protogalaxy is rotating, then we expect its initial collapse to occur first along the short axis followed by the intermediate and long axes, and resulting first in a planar or pancake structure (Zel'dovich 1970; Peebles 1980, chapter 20) followed by a prolate ellipsoid. We define t_{Cax} as the epoch at which the major axis a is longest compared to the other two, which should indicate the shell crossings of the shorter axes. For both turnaround and shell crossing, we use the median of the four methods as the final value ($\langle t_M \rangle, \langle t_C \rangle$ respectively), since the median minimizes the effects of single outliers.

5 RESULTS

In SPH simulations, centrally located gas particles in circular motion experience an artificial pressure due to the finite smoothing length of the hydrodynamic forces, and therefore tend to clump within the inner $\sim$1.5 smoothing radii from the centre, which typically represents the size of a galactic disc in this simulation. As such, in this study gas particles are used only to identify the most probable sites of galaxy formation, while dark matter dominates the overall dynamics and is therefore used exclusively in this analysis. Dynamical effects of the gas component on dark halo evolution will be addressed in Paper II. Furthermore, it is possible that the lowest mass galaxies ($M \lesssim 200$ DM particles) contain dynamical masses too small for stable numerical resolution. When applicable, we divide the sample of galaxies into subsets with $M > 200$ or $M > 1000$ DM particles, with the understanding that better-resolved galaxies should naturally provide more consistent results.

5.1 Collapse history

We first study the spatial evolution of each galaxy in our catalogue by following the particle list Γ from the initial to the final epoch. Figs 1 and 2 show the evolution of galaxies #12 and #22, containing 1776 and 703 DM particles respectively. It is evident from these two evolutionary sequences that the collapse is neither spherical nor homogeneous. Rather, the observed evolution, typical of all the galaxies in our catalogue, follows that predicted from the hierarchical-clustering scenario in the CDM model, in which a relatively isotropic distribution first collapses into small objects, which then subsequently accrete and virialize into the final bound galaxy.

5.1.1 Turnaround

As a predictive tool, the linear theory (equation 6) depends upon a reasonable determination of the turnaround time. Of the four methods listed in Section 4.5, the analytic method t_{Mz} predicts the turnaround epoch from only the initial conditions, while the others use measured quantities from the evolving simulation. In view of the facts that the initial particle distributions are non-spherical, that collapse is hierarchical, and that turnaround for an ellipsoidal distribution is ill-defined, it is essential to address whether the spherical-collapse model can provide any accurate determination of the turnaround time of a galaxy.

We present the computed turnaround and caustic crossing times for a variety of distinctly different evolutionary histories in Table 2. Galaxies #12 and #22 (well-behaved evolution, Section 5.2) are complimented with a large merger (#8) and galaxies #30 and #32, which suffer strong tidal encounters (Section 5.2.2). The respective four methods for determining each of these evolutionary epochs (described in Section 4.5) are all relatively consistent for the galaxies listed, independent of the large variation in collapse history.

Statistics for the full galaxy catalogue, as well as statistics for subsamples of 52 and 34 galaxies with well-behaved evolution (Section 5.2) are listed in Table 3. The first pair of data columns show that the mean dispersion between the epochs given by the four methods is relatively small ($\sim$0.4 Gyr) for turnaround and slightly larger ($\sim$1.4 Gyr) for caustic crossing. Recall from Section 4.5 that the final value $\langle t_M \rangle$ of turnaround (caustic-crossing) is the median of the four methods; the mean of these median values is given in the second pair of columns. A priori, we do not expect the turnaround (caustic crossing) epochs to be the same for all galaxies, hence the large dispersion in these values. The average caustic crossing time is nearly double that for turnaround, reflecting both our input assumption (Section 2) and that the spherical-collapse model is consistent with early post-turnaround evolution.

Downloaded from https://academic.oup.com/mnras/article-abstract/311/4/762/1746627 by California Institute of Technology user on 19 May 2020

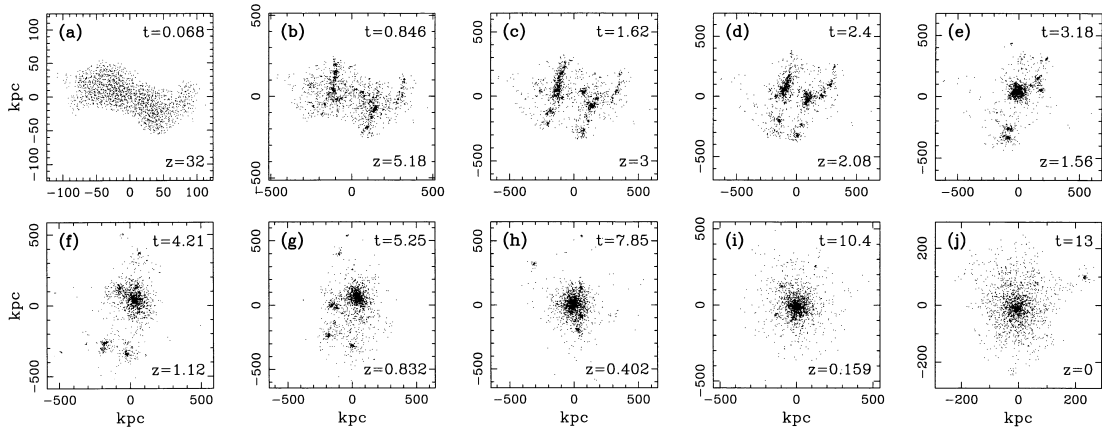

Figure 1. Particle positions plotted in physical coordinates and projected on to the Cartesian $(\hat{\imath}, \hat{k})$ plane for galaxy 12. The epoch is listed in Gyr in the upper right corner and the redshift in the lower right corner of each panel. Turnaround and crossing times correspond roughly to panels (c) and (e), respectively.

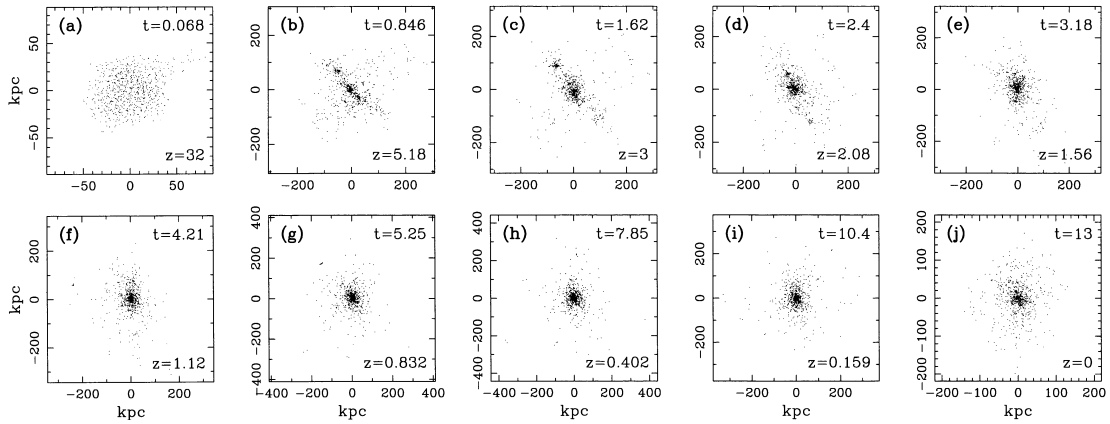

Figure 2. Same as Fig. 1 for galaxy 22. Turnaround and crossing times correspond roughly to panels (b) and (d) respectively.

Table 2. Sample turnaround and caustic crossing times.

Galaxy	Mass	t_{Md} t [Gyr]	$t_{M\delta}$ t [Gyr]	t_{Mz} t [Gyr]	$t_{M\%}$ t [Gyr]	$\langle t_M \rangle$ t [Gyr]
8	2431	2.92	2.66	2.92	2.92	2.92
12	1776	1.56	2.14	1.62	1.56	1.62
22	703	0.91	1.24	1.24	0.91	1.11
30	441	0.85	1.24	0.98	0.78	0.98
32	424	1.82	1.95	1.49	1.82	1.82
Galaxy	Mass	t_{Cto} t [Gyr]	$t_{C\delta}$ t [Gyr]	t_{Cax} t [Gyr]	$t_{C\sigma}$ t [Gyr]	$\langle t_C \rangle$ t [Gyr]
8	2431	5.77	6.55	2.66	4.73	4.73
12	1776	3.18	4.99	3.44	3.44	3.18
22	703	2.14	3.18	3.18	2.66	2.60
30	441	1.88	4.48	2.47	1.75	2.34
32	424	3.44	4.48	4.48	3.44	3.70

The last pair of columns in Table 3 give the average ratio of the median turnaround (caustic crossing) time to the analytic turnaround epoch t_{Mz}. That the average value of $\langle t_M \rangle / t_{Mz} \sim 1$ with very little dispersion shows that t_{Mz} is highly consistent with the empirical measures of turnaround; if we believe these latter three values, then the spherical-collapse model successfully predicts the turnaround epoch. Further, we find that the average caustic crossing time is nearly double t_{Mz}, also as expected. These tests support the applicability of the spherical-collapse model for determination of the turnaround and caustic crossing times.

In both Figs 1 and 2 one clearly observes that the particles pass through a planar or Zel'dovich (1970) pancake stage at extremely early times. Kuhlman, Melott & Shandarin (1996) find that the early collapse of the short axis and growth of the long axis are generic trends of particle distributions. EL95 also find that the short axis of a rotating ellipsoid typically collapses first into the expected sheet-like structure. This planar stage generally correlates closely with the predicted turnaround for a galaxy. Shell crossing occurs dramatically in galaxy #12 when the two pancakes collide, and more subtly in galaxy #22 as the intermediate axis collapses. After the collapse of the short axis, the galaxy still retains a significant quadrupole moment, since the quadrupoles are proportional to the difference between the squares of the axis lengths (Peebles 1969). Considering that the acquisition of angular momentum results from a coupling between the large-scale tidal field and the quadrupole moment of the galaxy, this coupling will remain significant until the longer axes have collapsed. We therefore expect the angular momentum in these non-spherical galaxies to increase beyond the spherically defined turnaround epoch. In the linear approximation (equation 7), we use only the initial values of the deformation and inertia tensors, having assumed that during linear evolution, the time-scales over which these tensors change are long compared to that of turnaround. As the axes collapse, the inertia tensor and hence the quadrupole

Downloaded from https://academic.oup.com/mnras/article-abstract/311/4/762/1746627 by California Institute of Technology user on 19 May 2020

Table 3. Statistics for t_M and t_C.

Catalog	$\overline{\sigma(t_M)}$	$\overline{\sigma(t_C)}$	$\overline{\langle t_M \rangle}$	$\overline{\langle t_C \rangle}$	$\overline{\langle t_M \rangle / t_{Mz}}$	$\overline{\langle t_C \rangle / t_{Mz}}$
All 77	0.38	1.39	1.54 ± 0.61	3.07 ± 1.07	1.13 ± 0.41	2.27 ± 0.71
LG 52	0.35	1.34	1.51 ± 0.61	3.00 ± 1.05	1.07 ± 0.33	2.17 ± 0.61
SE 34	0.34	1.38	1.48 ± 0.59	3.02 ± 1.09	1.02 ± 0.32	2.10 ± 0.64

Columns 2 and 3 give the average dispersion between the four epochs for determining t_M and t_C. Columns 4 and 5 list the average over each catalogue of the median values of the previous four epochs. Columns 6 and 7 list the average over each catalogue of the median epoch divided by the analytically determined t_{Mz}. See Section 4.5.

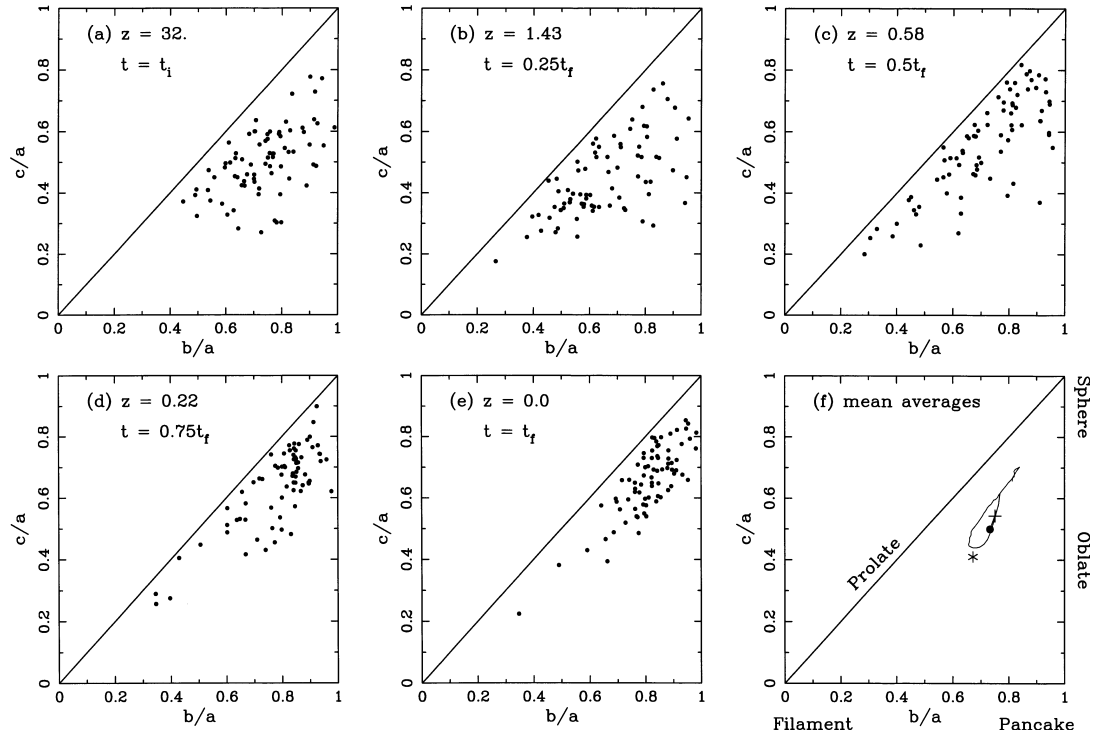

Figure 3. Distibutions of axis ratios for the full catalogue of galaxies at the (a) initial, (b)–(d) intermediate, and (e) final epochs. (f) The mean axis ratio for the full catalogue of galaxies is plotted for all epochs, starting at the solid dot. After a brief rise (motion with the Hubble expansion), the average galaxy collapses toward a pancake structure near turnaround (cross mark), then toward a prolate ellipsoid during shell crossing (star mark) and relaxes into a triaxial system. This figure may be compared with fig. 2 of Eisenstein & Loeb (1995).

moment will change strongly from its initial value, and it is therefore unclear whether we expect the growth of angular momentum near or beyond turnaround to continue linearly.

5.1.2 *Shape analysis*

To aid in studying the shape evolution of our galaxies, we define the morphological triaxiality parameter as given by Franx, Illingworth & de Zeeuw (1991),

$$T = \frac{a^2 - b^2}{a^2 - c^2}, \tag{17}$$

for which $T = 1$ is purely prolate and $T = 0$ is purely oblate. One may then classify galaxies with $0 < T < 1/3$ as oblate, $1/3 < T < 2/3$ as triaxial, and $2/3 < T < 1$ as prolate ellipsoids.

For initial conditions similar to ours, EL95 find their initial haloes to be prolate-triaxial. Given that the applicable collapse model is, to a better approximation, a collapsing ellipsoid rather than a sphere, we expect the following generic evolution of a galaxy: the initial prolate-triaxial particle distribution first expands linearly with the Hubble flow, and possibly becomes slightly more spheroidal. As the short axis collapses, the galaxy moves toward the oblate-pancake state, until the secondary axis collapses, at which point the galaxy evolves toward a prolate ellipsoid. At caustic crossing, the galaxy should pass through its most prolate distribution, after which virialization processes relax the system into an eventually spheroidal state. Unless a galaxy has suffered an extremely large merging event, in which case it is generally still relaxing or merging at the final epoch, our galaxies have generally accreted the majority of their clumps by roughly $t = \frac{1}{2}t_f$. Therefore we expect the galaxies to relax and virialize during the second half of the simulation.

We plot the evolution of the axis ratios in Fig. 3 for all 77 galaxies in our catalogue. This may be compared with fig. 2 of EL95, except that they evolve their galaxies only until the caustic crossing time. We see the expected initial quasi-spherical state (panel a) which evolves toward a prolate ellipsoid (panel b) and returns toward a spheroid (panels c–e). The mean values for the galaxies at each output are plotted in panel (f). Each galaxy evolves at its own rate, and so this latter panel is not a completely accurate representation of the axial history. None the less, we see

Downloaded from https://academic.oup.com/mnras/article-abstract/311/4/762/1746627 by California Institute of Technology user on 19 May 2020

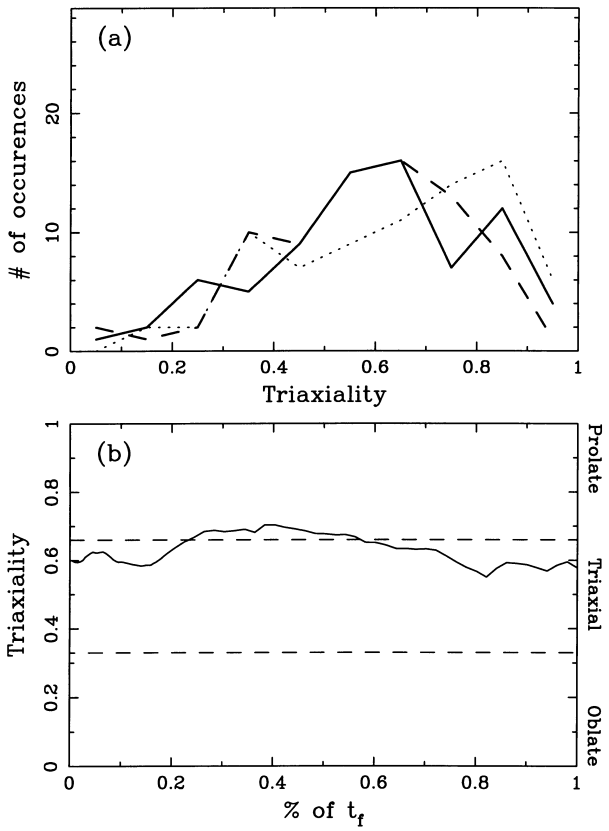

Figure 4. (a) Binned counts of triaxiality for the full galaxy catalogue at different epochs: t_i (solid curve); average epoch of caustic crossing ($t = 2.68$ Gyr; dotted curve); t_f (dotted curve). (b) Mean triaxiality for the full galaxy catalogue plotted versus epoch. The distribution is predominantly prolate at $1/4t_f$ and triaxial at t_f See Section 5.1.2.

the expected pattern from above. From the initial epoch, axial ratios briefly move toward the spheroidal state before collapsing toward first a pancake and then a prolate ellipsoid, after which they return toward a spheroidal distribution.

The evolution of the triaxiality parameter is presented in Fig. 4. Histograms of the triaxiality parameters are given in panel (a) for t_i, the average epoch of caustic crossing ($\langle t_C \rangle = 2.68$ Gyr) and t_f. The time evolution of the average values of the triaxiality parameters are given in panel (b). As expected, the initial galaxies are prolate-triaxial, and evolve to a more prolate state at caustic crossing. The final state of the galaxies is predominantly triaxial with a wide tail of both prolate and oblate ellipsoids. For comparison, Warren et al. (1992) find that their haloes are predominantly prolate. Dubinski (1994) finds that a coupling between the orbital distribution of dark matter and dissipative infall of gas (post-shell crossing) generally transforms a prolate-triaxial halo ($T \sim 0.8$) to an oblate-triaxial halo ($T \sim 0.5$), which we observe in Fig. 4(b). Dubinski further notes that the oblateness of the dark halo morphology constrains evolved haloes to have $b/a \gtrsim 0.7$, which we see in Fig. 3(f). Finally, he finds that the flattening c/a increases from roughly 0.4 to 0.6, which we also measure post-shell crossing, and which further agrees with deprojection analyses of observed elliptical galaxies $\langle c/a \rangle \sim$ 0.65–0.7 (Binney & de Vaucouleurs 1981; Franx et al. 1991; Frasano & Vio 1991; Ryden 1992).

Lastly, we find that the final shape of the galaxy has little or no dependence on the initial distribution, and therefore there does not appear to exist a bijective mapping between initial and final conditions. Furthermore, this implies that the mapping between Eulerian and Lagrangian descriptions of galaxies are unique to each particular galaxy and epoch.

5.2 Evolution of angular momentum

Sample plots of the total angular momentum ($L = |\boldsymbol{L}|$) evolution are shown in Figs 5 and 6. The five galaxies discussed in the previous section (#s 12, 22, 8, 30, 32) are displayed in panels 5(a)–(b) and 6(a)–(c) respectively. We have marked the four turnaround epochs and caustic crossing epochs (see figure caption for legend) on each curve. In galaxy #12, each quadruplet of points for both evolutionary epochs are nearly coincident. Despite the wide range of evolutionary histories in the remaining plots, the dispersion among these sets of points is quite small for each galaxy. This result supports the conclusions from Section 5.1.1 that our determination of these epochs is self-consistent and that the spherical-collapse model can quantitatively describe these highly non-spherical processes, including a wide mass range and interacting systems.

5.2.1 Qualitative comparison with linear theory

Linear theory coupled with the spherical-collapse model predicts that the angular momentum of an evolving galaxy will grow linearly until turnaround. From our discussion in Section 5.1.1 we expect the angular momentum to grow past turnaround and potentially until caustic crossing. Barring merging and accretion events, the angular momentum of a bound galaxy should remain constant in time thereafter.

We find that the expected model just described is only partially followed by the generic observed evolution of angular momentum. The normalized curves of $L(t)$ for seven galaxies have been overlayed in Fig. 5(c), and describe what we term the 'standard evolution.' $L(t)$ first rises linearly, up to and often beyond the turnaround epoch. The maximum value is reached near caustic crossing, after which the angular momentum turns over and slowly decays with time. 52 of our galaxies exhibit smooth linear growth of angular momentum before turnaround, and of these, 34 evolve according to the standard evolutionary sequence described in panel (c) (the remaining galaxies will be addressed shortly). We identify the 52 galaxies as the 'LG' catalogue (for linear growth) and the subset of 34 as the 'SE' catalogue (for standard evolution), while the 25 remaining galaxies are grouped in the 'INT' (for interacting, Section 5.2.2) catalogue.

The average time-dependence of L for the full, LG, SE and INT catalogues are given in Table 4. The pre-turnaround evolution of L scales as t to within 5 per cent. $L(t)$ deviates more strongly from linearity as it begins to turn over after t_M. On average, $L(t_C) \sim$ (2–3)$L(t_M)$ and, since $t_C \cong 2t_M$, the growth of L is still approximately linear [$L(t < t_C) \propto t^{0.85}$] between turnaround and caustic crossing. Given the possible non-spherical processes that could cause $L(t)$ to grow non-linearly at early times (examined in Section 5.1.2), it is doubly significant that the observed evolution of angular momentum so closely matches that predicted from linear theory, since this indicates that the considerable non-spherical processes have minimal effect during linear growth.

Simple physics dictates that the angular momentum of an isolated system must remain constant, and therefore if a post-turnaround galaxy is indeed largely insensitive to external tidal fields (Peebles 1980) and relatively isolated, we expect $L(t)$ to

Downloaded from https://academic.oup.com/mnras/article-abstract/311/4/762/1746627 by California Institute of Technology user on 19 May 2020

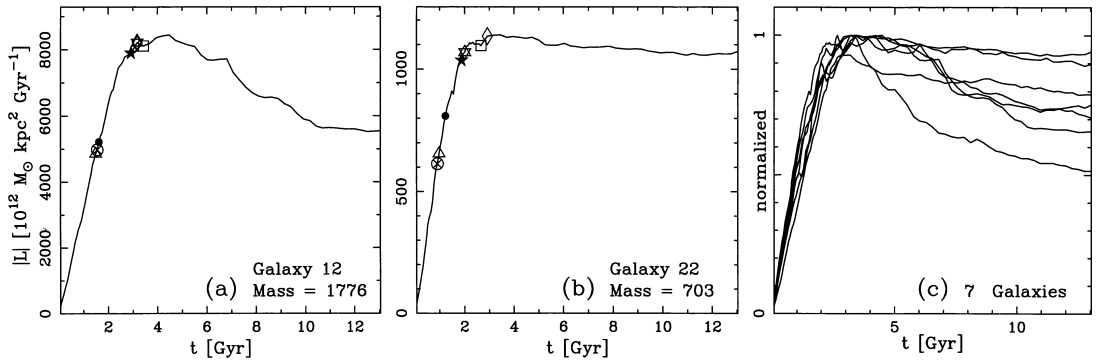

Figure 5. Total angular momentum versus epoch. (a) and (b) Examples of the 'standard evolution' of angular momentum, also marked with the measured turnaround and shell crossing epochs. (c) Overlay of seven normalized standard evolution galaxies. Note the general features of linear growth beyond turnaround, and the decay of angular momentum at later times. Small perturbations in the evolution correspond to minor tidal encounters with neighbours. Markers: cross = t_{Md}; triangle = $t_{M\delta}$; solid dot = t_{Mz}; open circle = $t_{M\%}$; solid star = $t_{C\sigma}$; diamond = t_{Cax}; open star = t_{Cto}; square = $t_{C\delta}$.

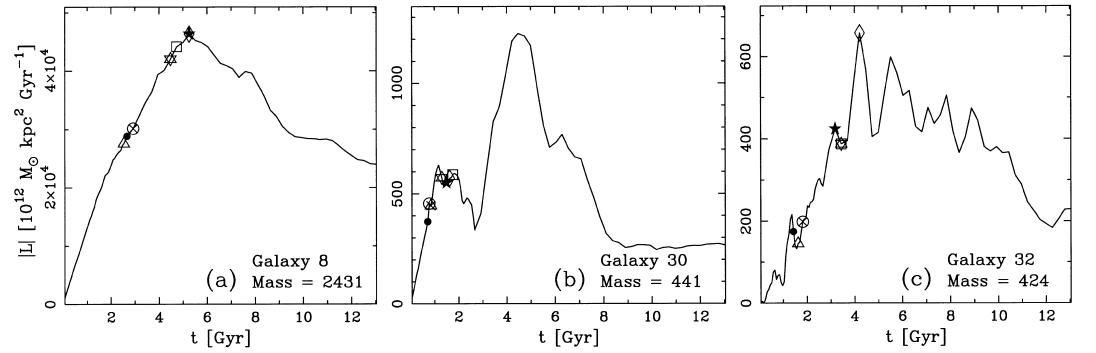

Figure 6. Notation as in Fig. 5. (a) A heavily merging system. (b) and (c) Galaxies suffering large-scale and repeated tidal encounters.

Table 4. Average $\langle\beta\rangle$ in $L \propto t^{\beta}$.

Catalog	β until t_M	$\frac{1}{2}(t_M + t_C)$	β until t_C
All 77	0.93 ± 0.14	0.87 ± 0.16	0.83 ± 0.16
LG 52	0.95 ± 0.10	0.90 ± 0.13	0.84 ± 0.14
SE 34	0.95 ± 0.09	0.90 ± 0.13	0.84 ± 0.14
INT 25	0.90 ± 0.18	0.83 ± 0.21	0.79 ± 0.23

remain roughly constant for $t \gtrsim t_M$ for spherical collapse, and $t \gtrsim t_C$ for ellipsoidal collapse. Rather, we find the general trend, as seen in Fig. 5 (and in nearly every galaxy in our full catalogue), that the measured angular momentum decays after shell crossing. BE87 also find this trend in their simulations, and attribute it to the loss of angular momentum to surrounding material during merging and 'highly non-linear evolution.'

We examined the mechanism for loss of angular momentum by studying galaxies for which we had not culled out unbound particles after running the FOF group-finding algorithm. After t_C, the decay of angular momentum is much more pronounced. Identically, in galaxies for which we exclude a subset of the outermost bound particles, the angular momentum also decreases more strongly with time. Since it is computationally too expensive to determine *every* bound particle within a group (Section 3.2), it is expected that we will not identify every particle bound to a given system using our group-finding technique. Each gravitationally bound galaxy contains particles at radii greater than our effective overdensity cut-off which have not been included in our catalogue, and to which significant amounts of angular momentum are transferred after shell crossing and during relaxation. This transfer of angular momentum from triaxial distributions to outlying particles is expected through Landau damping in self-gravitating systems. Unless every particle bound to a group can be identified, the apparent decay of the measured angular momentum will be a general trend of numerical simulations.

5.2.2 *Effects of the local tidal field*

The question still remains why 43 of our 77 galaxies which pass the original selection criteria do not have angular momenta matching the standard evolution model [due to noisy $L(t \gtrsim t_C)$], and why 25 of these have angular momenta which are not smoothly linear at early times. As an approximate study of the evolution of the tidal field, we compute the torque on each galaxy by every other galaxy in the simulation (a short N^2 calculation, since there are only 98 identified groups). Substituting the first three terms of the Taylor expansion of the potential into the torque integral and simplifying, we find

$$\tau_i = \epsilon_{ijk} T_{jl} \mathcal{I}_{lk}, \tag{18}$$

where $\mathcal{I}_{jk}$ is the inertial tensor (equation 8 and Dubinski 1992).[2]

$$T_{ij} = G \sum_{\alpha} m_{\alpha} \frac{3x_i^{\alpha} x_j^{\alpha} - \delta_{ij} r_{\alpha}^2}{r_{\alpha}^5}. \tag{19}$$

[2] It follows that for a potential field ψ, $T_{ij} = [3\partial_i\partial_j - \delta_{ij}\nabla^2]\psi$ from which we see directly that the the deformation tensor (equation 7) is directly related to the gravitational tidal tensor, since the diagonal elements of both tensors do not contribute to the antisymmetric tensor product with the inertial tensor (CT96).

Downloaded from https://academic.oup.com/mnras/article-abstract/311/4/762/1746627 by California Institute of Technology user on 19 May 2020

Since we are not measuring the torque due to the full mass distribution in the simulation, we do not expect τ to remain constant before turnaround, as would be expected from the linear growth of L. Conversely, for a universe consisting of only two galaxies with fixed comoving separation and no other external tidal forces, we expect the torque to decay as $\tau \propto t^{-2}$.

The torque acting on a typical galaxy in the SE catalogue roughly follows a t^{-2} decay superposed with small perturbations ($\lesssim$50 per cent) reflecting weak encounters with neighbours, generally at large distances [$\gtrsim$(1–2) Mpc]. These typically correspond to low-level ($\lesssim$10 per cent) fluctuations in the angular momentum, especially during late times ($t \gtrsim t_C$). Intuitively, these are the expected conditions for relatively isolated field galaxies. Since the roles of the tidal field and induced shear in the quasi- and non-linear regimes of these galaxies are not negligible, models of single systems (e.g. Zaroubi, Naim & Hoffman 1996) should explore the quantitative effects of inclusion versus exclusion of tidal interactions.

Naturally, however, not all galaxies will exist in the 'field.' Every galaxy excluded from our SE catalogue suffers strong (1–2 orders of magnitude) and repeated tidal interactions with neighbouring galaxies. The angular momenta of these galaxies can vary by as much as 50 per cent over 1–2 Gyr periods throughout the entire simulation. These are galaxies expected to be found in groups or clusters, with the most massive examples representing the central members. Galaxy 30, shown in Fig. 6(b), orbits within a few hundred kpc of a galaxy three times as massive, while suffering minor encounters with comparably sized galaxies at distances of 1–2 Mpc. While the late-time evolution is highly erratic, the early growth of L is still linear. Galaxy 32, shown in panel (c), suffers two close encounters with galaxies three and five times as massive. Here, the rapid variations in L appear quasi-periodic, most likely reflecting the rotational frequency of the galaxy.[3] Even in this extreme case, the growth of L is still linear at early times, though heavily polluted due to the effects of early tidal interactions. This is the case with all 25 galaxies in the INT catalogue (hence the name 'interacting'). Despite the noisy early evolution, the average pre-turnaround angular momentum grows as $t^{0.928}$ (see Table 4) for these galaxies. Therefore, even in the rich tidal environment of clusters, we find (quasi)linear growth of L at early times, indicating that the local tidal field is not negligible, but that the effects do not become dominant until local evolution becomes non-linear.

We also expect that galaxies may suffer tidal interactions from the outermost shells of their own infalling matter. In galaxies originating from higher-ν peaks (defined in Section 4.3), the matter in the immediately surrounding low-ν region will have a density similar to that of the collapsing object at early times. According to the formalism of the spherical-collapse model, this corresponds to a mass shell of $\Omega \gtrsim 1$ but $< \Omega_{\rm galaxy}$. This shell will follow the collapse of the galaxy, and will evolve into surrounding matter that is closer than its initial comoving distance, generating more torque than expected from linear theory (EL95). Even our most isolated galaxies still undergo small fluctuations in L and τ, indicative of the tidal influences of the most closely neighbouring environs. Also, in systems with significant substructure, small-scale motions in non-linear regions and torques caused by nearby structure can effect large changes in internal angular momentum (BE87). We see this in a few of the more massive of the galaxies with noisy $L(t \gtrsim t_C)$, where small satellites with eccentric orbits efficiently transfer angular momentum out of the central system to the surrounding matter. However, even when the distributions are non-linear at early times, we still find exceptionally good agreement with the qualitative predictions of linear-growth theory.

[3] L is expected to vary at roughly twice the rotational frequency of the torqued object. This is also seen in the tidal interactions of binary stars.

5.3 Quantitative comparison with linear theory

The predictive capacity of linear theory of tidal torques was partially examined by BE87, who computed the predicted final value by measuring the initial $L_{\rm i}$ for each galaxy and evolving it forward to $a = 3$ using the linear time factor such that $L_{\rm pred} = a^2 \dot{D} L_{\rm i}$. They then compared this semi-empirical prediction with the actual final angular momentum, and found that the predicted final value tends to be a factor of $\sim$3 larger than the actual $L_{\rm f}$ with a total scatter about the mean of roughly the same factor. This method failed to test the linear theory fully, since it improperly assigned the same turnaround epoch to every galaxy, and relied on the actual initial spin, rather than the rotation predicted from the external tidal field.

To test the linear-theory predictions properly, we evaluate the initial conditions using the initial tidal and inertia tensors, as prescribed in Section 4.4, and directly compare the resulting values of $L^{(1)}$ (equation 6) to the actual total angular momentum at each galaxy's individual turnaround and caustic crossing epochs, as well as to the final value $L_{\rm f}$. Since the later-time decay of angular momentum can range from slightly noisy for the SE catalogue to strongly varying in the INT catalogue (discussed in the previous subsection), the value of the angular momentum at the final epoch $L(t_{\rm f})$ may prove sensitive to which epoch we chose to label as 'final.' We use two methods to approximate the final value $L_{\rm f}$ for a smooth decay of angular momentum. We extrapolate a linear least-squares fit for $L(t > t_C)$ to find $L_{\rm f}^{\rm lin}$, and also smooth the angular momentum over time using a 16-point Savitzky–Golay filter (Press et al. 1992) to find $L_{\rm f}^{\rm sm}$. This algorithm does not require symmetric smoothing, hence its applicability.

In Fig. 7 we plot galaxy mass versus the ratio of the predicted to actual angular momentum for the full catalogue, using different symbols for the LG, SE and INT galaxies. Corresponding histograms for these ratios are shown in Fig. 8. We first address the value of predicted to actual angular momentum at turnaround (panel a of both figures). The distribution of $L^{(1)}/L$ at t_M peaks at a ratio of $\sim$1–2 with a significant tail to larger values. $L^{(1)}(t_M)$ generally overestimates the actual value $L(t_M)$ for a given galaxy by $\sim$3–4, with a dispersion of roughly 50–70 per cent. BE87 also found the same degree of overestimation with a larger scatter about the mean. Since caustic crossing, rather than turnaround, is the epoch at which angular momentum ceases to grow, we also test the correlation of $L^{(1)}/L$ at t_C. The distribution appears similar to those in Figs 7 and 8, yet with a mean ratio roughly 1 larger than, and dispersion equal to, that for turnaround. We previously noted that the growth of $L(t_M < t < t_C)$ deviates slightly from linearity. However, in general $L(t_C) \sim$ (2–3)$L(t_M)$. Considering that $L^{(1)}$ grows linearly and also that $t_C \simeq 2t_M$, we expect the average value of $L^{(1)}/L$ to be systematically larger at t_C than at t_M, yet with a roughly comparable dispersion.

Angular momentum is approximately conserved in the post-turnaround era, indicating that $L(t_M)$ should correlate closely with $L_{\rm f}$. If the linear-theory prediction of $L^{(1)}$ at turnaround does not correlate with the final angular momentum of an evolved galaxy, then the applicability of the linear theory is drastically reduced. We show the ratio of the predicted angular momentum at

Downloaded from https://academic.oup.com/mnras/article-abstract/311/4/762/1746627 by California Institute of Technology user on 19 May 2020

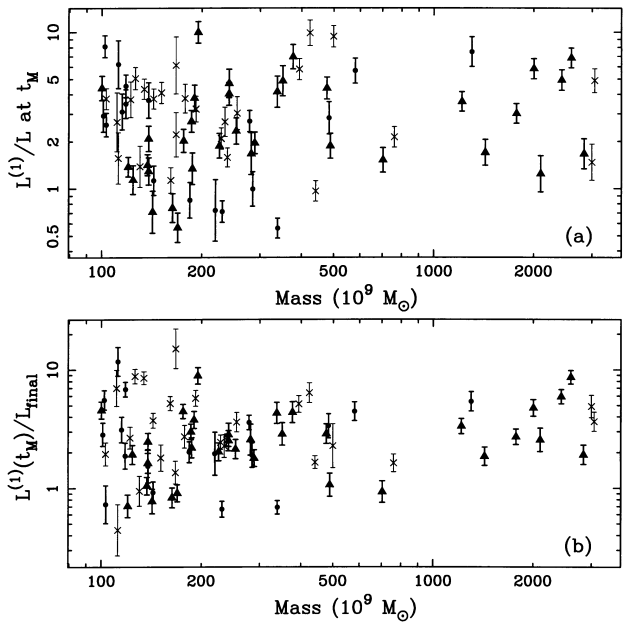

Figure 7. (a) Predicted versus actual total angular momentum at turnaround. (b) Predicted angular momentum at turnaround versus final actual angular momentum. Both distributions are centred about ~3, with a ~70 per cent dispersion. Crosses denote the excluded (INT) catalogue, triangles indicate members of the LG catalogue *only*, and circles indicate members of the SE catalogue (LG implicit).

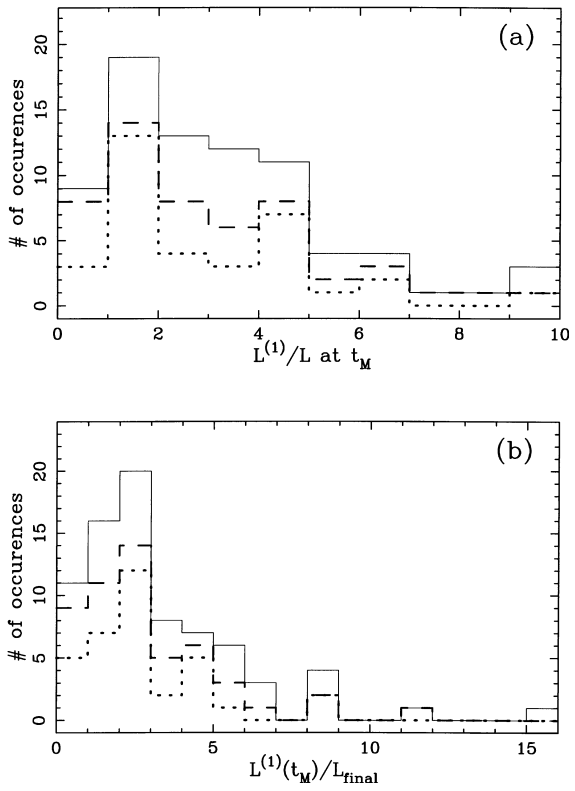

Figure 8. Binned histograms corresponding to ratios plotted in Fig. 7. The solid curve denotes all galaxies, the dashed curve denotes galaxies with $M \geq 200$, and the dotted curve those galaxies with $M \geq 1000$ particles.

turnaround to the final actual angular momentum $L^{(1)}(t_M)/L_f$ in panel (b) of Figs 7 and 8. The distribution is highly peaked about ~2–3, again with a significant tail to higher values, but with more power in the lesser values as well. Given the typical stochastic decay of $L(t > t_C)$ seen in simulations, we expect both the mean [since $L^{(1)}(t_M) > L(t_M) > L_f$] and variance (since the decay rate is different for each galaxy) of this distribution to be higher than when comparing $L^{(1)}/L$ at t_M. In fact, we find that the mean and dispersion for both ratios are nearly identical. We find similar results by replacing L_f with L_f^{lin} and L_f^{sm}. If one approximates the decay of L as an inherently smooth function of time, then the tidal noise superposed on that decay is generally only of the order $\lesssim$10 per cent. Even for galaxies with 50 per cent variation in $L(t)$, the linear fit and smoothed value of L_f typically differ from the true final value by $\lesssim$15 per cent. Accordingly, the average ratios for these three methods differ by roughly the same factor. We conclude that L_f^{lin} and L_f^{sm} are consistent methods of approximating the final angular momentum. There is little gained in using these two methods to determine L_f. However, the smoothed angular momentum damps out large variations in tidally disturbed galaxies and thereby allows a more consistent estimation of the underlying angular momentum evolution at late times, while the linear fit permits one to extrapolate beyond the limits of the simulation.

Provided the measured L did not decay at later times, one would expect the final value L_f to be roughly equal to the angular momentum at caustic crossing, as seen in galaxy #22 (Fig. 5b). We examine the ratio of $L^{(1)}(t_C)/L_f$, and find a peak value of ~(4–5), again with a dispersion of 50–70 per cent. The mean is again larger, since $L^{(1)}(t_C) > L^{(1)}(t_M)$. While caustic crossing may prove itself more useful than turnaround in linear theory of collapsing ellipsoidal distributions, it does not provide any increase in accuracy and cannot be properly implemented until we efficiently circumvent the numerical decay of angular momentum.

Averages for the six ratios discussed and all four galaxy catalogues are listed in Table 5. We further discriminate between galaxies with masses $M > 200$ and $M > 1000$ particles for each catalogue, in the event that correlations are mass-dependent. Each average ratio is listed with the per cent dispersion about the mean. The deviation about the mean is higher when including the lowest mass ($M < 200$) objects, since these have poorer numerical resolution. We also find that the average ratios for subsets of galaxies with $M > 1000$ are typically larger than subsets also containing lighter galaxies ($M > 200$ and $M > 0$). As seen in Fig. 7, less massive objects exhibit stronger scatter toward the lower end of the ratio scale, which lowers the average and raises the dispersion. The distributions of these points have roughly the same peaks and high-end tails for the different catalogues (Fig. 8). Thus the average and scatter about the mean are generally comparable between catalogues for the same mass-scale. Except for the mean ratios at caustic crossing, which have systematically larger values, the mean and dispersion values for all the tests are highly consistent, indicating that $L^{(1)}$ is well correlated with both $L(t_M)$ and L_f.

Previous studies (White 1984; BE87) also conclude that linear theory overestimates L by a factor of ~3. We find a scatter about this mean of roughly 70 per cent for low-mass objects and 50 per cent as the mass-scale is increased. Since our largest objects show stronger correlations, we expect that improvements in resolution will further tighten the correlation between actual and predicted angular momentum.

Downloaded from https://academic.oup.com/mnras/article-abstract/311/4/762/1746627 by California Institute of Technology user on 19 May 2020

Table 5. Average values for $L^{(1)}/L$.

	$M>$	N	$\frac{L^{(1)}(t_M)}{L(t_M)}$	$\frac{L^{(1)}(t_C)}{L(t_C)}$	$\frac{L^{(1)}(t_M)}{L(t_t)}$	$\frac{L^{(1)}(t_M)}{L^{\rm lin}(t_t)}$	$\frac{L^{(1)}(t_M)}{L^{\rm sm}(t_t)}$	$\frac{L^{(1)}(t_C)}{L(t_t)}$
Full	0	77	2.85 (0.70)	3.87 (0.74)	3.10 (0.70)	2.69 (0.72)	2.89 (0.75)	5.73 (0.75)
	200	39	3.17 (0.71)	4.25 (0.61)	3.11 (0.62)	2.87 (0.59)	3.00 (0.64)	5.73 (0.62)
	1000	11	3.79 (0.62)	4.98 (0.48)	4.47 (0.54)	4.29 (0.54)	4.41 (0.54)	8.18 (0.45)
LG	0	52	2.58 (0.73)	3.61 (0.73)	2.72 (0.72)	2.50 (0.72)	2.54 (0.73)	5.08 (0.75)
	200	28	2.97 (0.70)	4.04 (0.66)	2.90 (0.67)	2.72 (0.63)	2.83 (0.66)	5.26 (0.67)
	1000	9	3.97 (0.62)	5.04 (0.49)	4.32 (0.60)	4.11 (0.59)	4.34 (0.59)	8.12 (0.48)
SE	0	34	2.61 (0.71)	3.61 (0.67)	2.73 (0.69)	2.51 (0.68)	2.60 (0.70)	3.51 (0.70)
	200	20	3.31 (0.56)	4.49 (0.45)	3.17 (0.60)	2.86 (0.57)	3.00 (0.59)	5.45 (0.52)
	1000	8	3.69 (0.63)	4.17 (0.63)	4.17 (0.63)	3.91 (0.60)	4.06 (0.62)	6.87 (0.47)
INT	0	25	3.51 (0.61)	4.81 (0.76)	4.05 (0.59)	3.26 (0.68)	3.80 (0.72)	7.87 (0.66)
	200	11	3.66 (0.74)	5.03 (0.43)	3.60 (0.48)	3.26 (0.48)	3.39 (0.62)	6.95 (0.45)
	1000	2	3.20 (···)	4.32 (···)	5.17 (···)	5.22 (···)	4.77 (···)	8.88 (···)

Averages are listed with the respective fractional dispersions in parentheses.

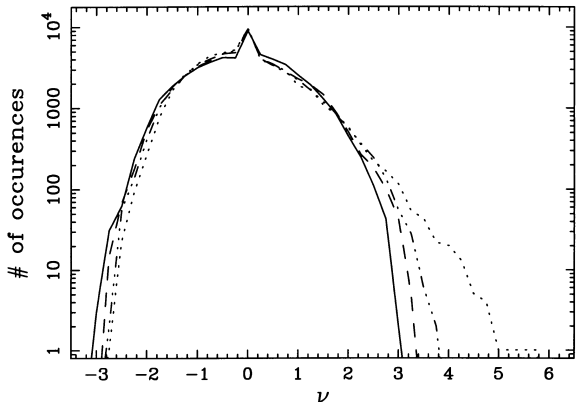

Figure 9. Binned histogram of peak height ν for 50 000 randomly placed spheres containing 2500 (solid curve), 1000 (dashed curve), 500 (dot-dashed curve) and 100 (dotted curve) particles.

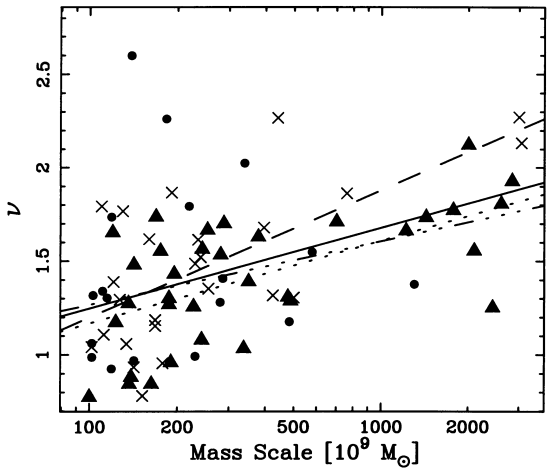

Figure 10. Peak height ν versus mass-scale for the same catalogues as Fig. 7. Also plotted are the least-squares linear interpolations for the full (solid curve), LG (dot-dot-dot-dashed curve), SE (dotted curve) and INT (dashed curve) catalogues.

5.4 Peak heights

Following the biased galaxy-formation scheme (Kaiser 1984; Politzer & Wise 1984; Peacock & Heavens 1985; Bardeen et al. 1986), we expect that galaxy formation occurs only for density peaks above a given threshold of the initial Gaussian density field. The relative peak height above the underlying fluctuation of the density field is characterized by $\nu = \delta/\sigma$, where σ is determined for the mass-scale of the galaxy in question. Since evolving peaks are subject to strong tidal fields, not every high-ν peak is guaranteed to evolve into a galaxy. Rather, peaks can be stretched or sheared such that the highest-ν regions fail to undergo infall while lower-ν peaks collapse into bound structures (van de Weygaert & Babul 1994; EL95). Rather than assume that all our galaxies originated from the highest-ν peaks, we have the luxury of tracing back the final bound structures to the initial density field to test the correlation of peak height with collapse.

For a CDM power spectrum, as the mass-scale increases, the deviation σ will decrease, since larger volumes more closely approximate the background density. Furthermore, low peaks on a high mass-scale become higher mass peaks when measured on lower mass-scales. We expect that as the mass-scale increases, both the maximum peak height and the frequency of occurrence of the highest peaks will decrease. We tested this by measuring ν at 5×10^4 randomly placed points for mass-scales of 2500, 1000, 500 and 100 particles. We found $\sigma = 6.95 \times 10^{-2}$, 8.68×10^{-2}, 0.103, 0.145 respectively, indicating that σ is anticorrelated with the mass-scale M. Histograms for these essays are plotted in Fig. 9. All four mass-scales have nearly the same distribution for $\nu < 2$. As the mass-scale decreases, the maximum peak height increases as well as the number of high-ν peaks encountered, as predicted.

From these findings, one might be led to conclude that ν should vary inversely with mass-scale, such that more low-mass galaxies should originate from high-ν peaks. There are two effects which lead to the opposite correlation. First, low-ν peaks on high mass-scales are likely to contain, and to be identified with, a galaxy arising from a higher-ν peak on a smaller mass-scale. Second, the high-ν peaks on small mass-scales evolve quickly and become lower-ν peaks on higher mass-scales. Both effects tend toward medium-ν peaks on medium mass-scales, and a deficit of low-ν, high-mass peaks as well as high-ν, low-mass peaks. That implies a correlation of higher peak height with mass-scale.

We find values of ν between 0.7 and 2.6 for the full catalogue, with the lowest and highest peaks being the rarest. In Fig. 10 we plot the distribution of ν versus mass-scale for the four catalogues, accompanied by the best-fitting lines for each catalogue. On average, ν is larger for higher-mass galaxies and there are relatively few high-ν, low-mass galaxies, as postulated above. Furthermore, the distribution of moderate-mass objects is spread over a wide range of values of ν, with very few peaks >2. This may also be a consequence of the 'migration' scenario described

Downloaded from https://academic.oup.com/mnras/article-abstract/311/4/762/1746627 by California Institute of Technology user on 19 May 2020

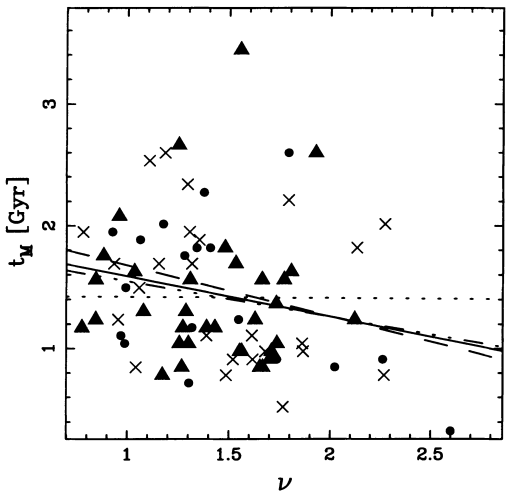

Figure 11. As in Fig. 10, but plotting turnaround time versus peak height ν.

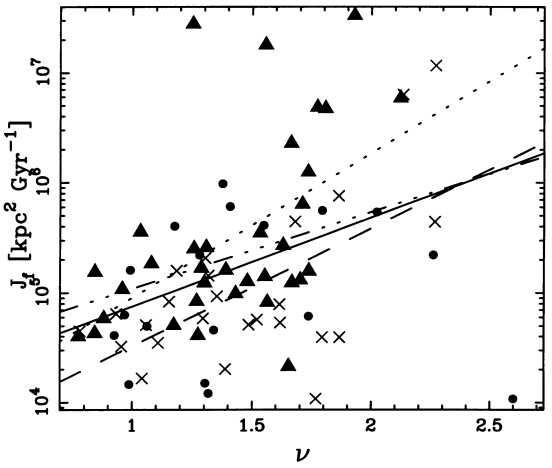

Figure 12. As in Fig. 10, but plotting specific angular momentum versus peak height ν.

above, which makes low-ν, high-M and high-ν, low-M galaxies comparatively rare. This underlines that biasing is a function of scale. For a high-mass distribution to evolve into a high-mass galaxy, it appears that it must come from a larger peak density region, otherwise the outer mass shells do not collapse and the object evolves into a lower-mass galaxy.

From equation (16), we find that the turnaround time for a galaxy scales as $t_M \propto \delta_i^{-2/3}$. As ν increases, the time a galaxy spends in the linear regime decreases. We plot ν versus turnaround time in Fig. 11, in which we have also plotted the best-fitting lines for all four catalogues. In all cases, t_M appears to vary inversely with ν, as expected. Since a galaxy acquires most of its angular momentum through tidal interactions before turnaround, this implies that higher-ν objects should gain less angular momentum (Hoffman 1986). We plot the specific angular momentum $J \equiv L/M$ versus ν in Fig. 12, again complemented with best-fitting lines for the four catalogues. Instead, we find the moderate trend that angular momentum increases with increasing peak height, most drastically for the SE galaxies. If one considers the peaks scenario, higher peaks tend to be more strongly clustered (Kaiser 1984; Bardeen et al. 1986), implying that high peaks evolve in environments within stronger local tidal fields. Even though these objects spend less time in the linear regime, the local tidal field

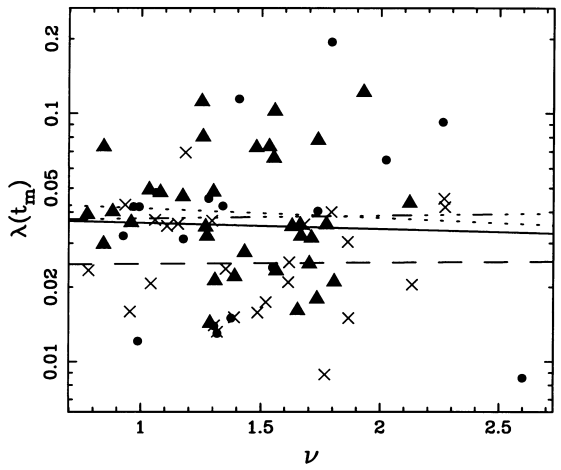

Figure 13. As in Fig. 10, but plotting spin parameter λ versus peak height ν.

must have a more significant effect. CT96 also find, from angular-momentum probability distribution functions derived from linear theory, that higher-ν peaks tend to having higher L.

A common measurement is the dimensionless spin parameter $\lambda = LE^{1/2}/GM^{5/2}$. Due to the problem outlined in Section 5.2.1 in identifying all bound particles within a group, uncertainty in the particle make-up of a galaxy affects all three measurables in λ. Given this caveat, we examined the spin parameter measured at turnaround and the final epoch versus peak height. It is expected (e.g. Hoffman 1988; HP88) that λ and ν will be anticorrelated for galaxies arising from a random density-field. The distributions are displayed in Fig. 13, and show no meaningful correlations other than a mean around $\lambda \sim 0.05$ with an appreciable scatter, which is consistent with previous findings (e.g. BE87; HP88). Given the large uncertainties that enter into λ, this result suffers from the limited size of our sample. We will reexamine the $\lambda - \nu$ anticorrelation with our larger data set in Paper II.

CT96 calculate the equiprobability contours for mass and specific angular momentum for a CDM power spectrum, on to which they superpose (their fig. 9) observations by Fall (1983) for the masses and specific angular momenta of luminous elliptical, Sb and Sc galaxies. Spirals are generally constrained within the contour limits, but do not follow the slope of the probability distributions. The elliptical galaxies mostly lie outside the high probability contours, and also exhibit a discrepant slope. We display the equiprobability contours for peaks with height $1/2 \leq \nu < 3/2$ and $3/2 \leq \nu \leq 5/2$ from CT96, superposed with data from our galaxy catalogue, separated into galaxies with $\nu < 1.5$ and $\nu \geq 1.5$, in Fig. 14. Both sets of galaxies are very well constrained within the corresponding contours, although the locus of points for $\nu < 1.5$ lies off-centre from the probability maximum. Since the probability distribution functions of CT96 have been derived from equation (6), this excellent match lends validity to the use of ensemble averages derived from linear theory.

5.5 Scalings

In the previous section we found that the final value of the angular momentum L_f roughly equals that at turnaround, as predicted by linear theory. This value can be estimated from equation (6) using the turnaround condition $\delta = 1.07$ (equation 10). This condition can be written equivalently as $\delta = -D(t_M)\nabla^2\psi$, from which the

Downloaded from https://academic.oup.com/mnras/article-abstract/311/4/762/1746627 by California Institute of Technology user on 19 May 2020

previous relation yields the equivalent condition $D_M \simeq 1/\nabla^2\psi$, where $D_M = D(t_M)$. Denoting the initial mass and radius of the protogalaxy by M and R_0 respectively, we insert this into equation (6) (White 1994; CT96),

$$L_{\rm f} \sim a_M^2 + \dot{D}_M \nabla^2\psi M R^2 = a_M^2 \frac{\dot{D}_M}{D_M} M R_M^2 \propto \frac{\dot{D}_M}{D_M}\rho_{{\rm b},M}^{-2/3} M^{5/3}$$
$$\propto \left(\frac{a_M \dot{D}_M}{\dot{a}_M D_M}\right)\frac{\dot{a}_M}{a_M}\rho_{{\rm b},M}^{-2/3} M^{5/3} \propto \Omega^{0.6} H(\Omega H^2)^{-2/3} M^{5/3}$$
$$\propto \Omega^{-0.07}\left(\frac{\dot{a}_M}{a_M}\right)^{-1/3} M^{5/3}, \qquad (20)$$

where in the last step we have used the approximation given by Peebles (1993, equation 5.120). For an Einstein–de Sitter universe, $a \propto t^{2/3}$ and $\Omega = 1$, and the previous expression simplifies to

$$L_{\rm f} \cong L(t_M) \propto t_M^{1/3} M^{5/3}. \qquad (21)$$

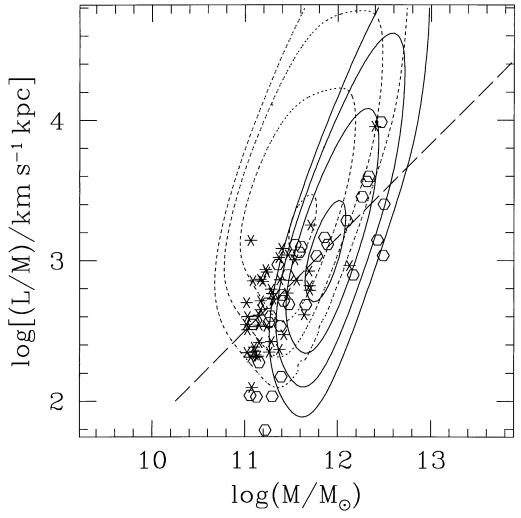

Figure 14. Mass versus specific angular momentum for the galaxies with $\nu < 1.5$ (six-point stars) and $\nu \geq 1.5$ (open hexagons), superposed on theoretical equiprobability contours from fig. 9 of CT96, corresponding to peaks with height $1/2 \leq \nu \leq 3/2$ (dotted contour) and $3/2 \leq \nu \leq 5/2$ (solid contour). The dashed line indicates the scaling $L/M \propto M^{2/3}$.

From a physical standpoint, we expect objects with larger masses to gain a greater final angular momentum, not only due to the linear mass term in the basic expression for $L(t)$, but also since larger masses tend to fill larger volumes, whereby more massive galaxies will have larger moment arms on which the tidal field will act. Additionally, the longer the tidal field acts upon an object, the greater the acquired angular momentum; hence the dependence on the time at which angular momentum stops growing. However, since the turnaround time is a function of overdensity (hence mass), the time dependence in equation (21) is not fully given by $t_M^{1/3}$.

We test equation (21) directly in Fig. 15, in which we have plotted $L_{\rm f}$ versus $M^{5/3}$ and $t_M^{1/3}M^{5/3}$ for all four galaxy catalogues. With a correct scaling, the distribution of points will be linear. We find that the scaling $L_{\rm f} \propto t_M^{1/3}M^{5/3}$ yields the smallest χ^2 residual and also has the most linear distribution in all four catalogues.

To more properly test the validity of these scalings, we must see if they naturally occur in the data. We use the singular value decomposition (SVD) method of generalized least-squares fitting (Press et al. 1992) to solve for the power-law exponents by rewriting equation (21) as a linear combination of logarithms

$$\log L_{\rm f} = \log(\text{constant}) + \alpha \log M + \beta \log t_M. \qquad (22)$$

Since the growth of angular momentum continues past turnaround and up until crossing time t_C, we fit equation (22) for t_C as well as t_M. Selected results are listed in Table 6. We find that $L_{\rm f}$ scales with mass $M^{1.5-1.75}$, which is highly consistent with an $M^{5/3}$ dependence. The scalings in turnaround and caustic crossing time both vary inconsistently, and differ from the $t^{1/3}$ dependence, as expected from our discussion above. At present, our findings remain inconclusive regarding the temporal factor in equation (21). Considering that our galaxies cover more than a decade in mass, whereas the turnaround times typically differ by less than 40 per cent, it is not surprising that $L_{\rm f}$ scales predominantly on the mass. It is perhaps more surprising that the empirically determined mass scaling so closely matches linear theory.

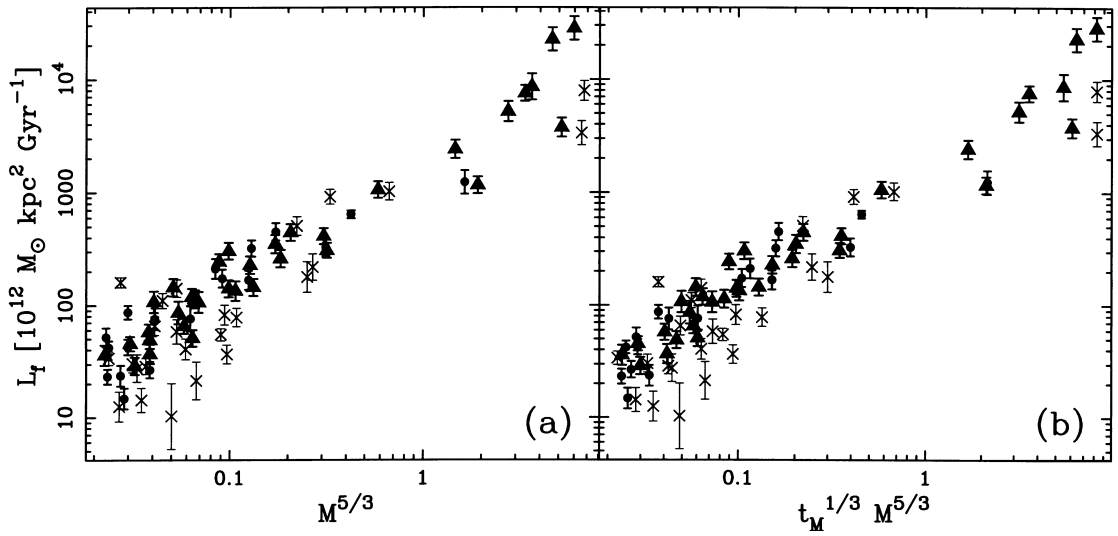

Figure 15. Final angular momentum for the same catalogues as Fig. 7 versus scalings determined from equation (6). (a) $L_{\rm f} \propto M^{5/3}$. (b) $L_{\rm f} \propto t_M^{1/3}M^{5/3}$ (the best χ^2 residual for all catalogues).

Downloaded from https://academic.oup.com/mnras/article-abstract/311/4/762/1746627 by California Institute of Technology user on 19 May 2020

Table 6. Scaling parameters for SVD fitting.

			M^α		$M^\alpha t_M^\beta$			$M^\alpha t_C^\beta$		
	$M>$	N	α	χ^2	α	β	χ^2	α	β	χ^2
Full	0	77	1.76	2.63	1.67	0.645	2.21	1.71	0.595	2.36
	200	39	1.72	2.26	1.63	0.481	2.10	1.64	0.394	2.18
LG	0	52	1.76	1.55	1.66	0.595	1.22	1.70	0.498	1.38
	200	28	1.67	1.57	1.59	0.446	1.43	1.61	0.295	1.53
SE	0	34	1.76	1.43	1.64	0.772	1.09	1.70	0.523	1.28
	200	20	1.75	1.72	1.47	1.09	1.22	1.55	0.821	1.49

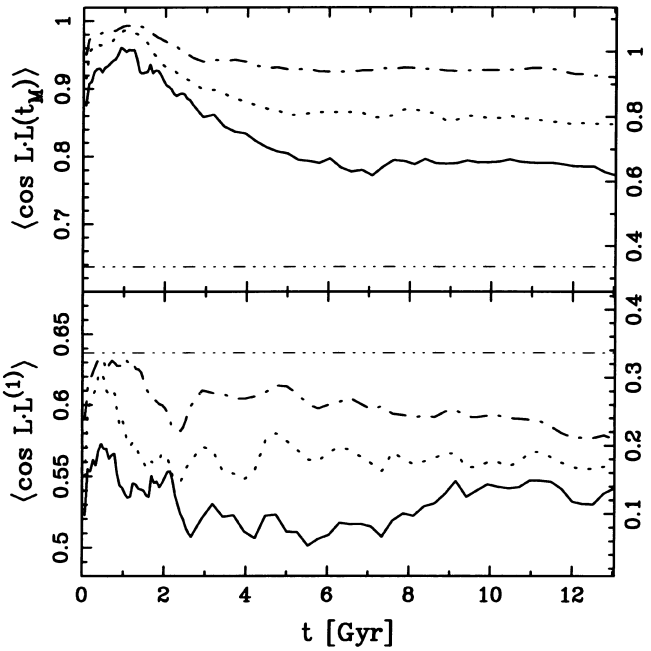

Figure 16. Average inner products of spin vectors in time. An uncorrelated distribution will remain at $2/\pi = 0.64$, marked by the dot-dot-dot-dashed line. The right-hand abscissa indicates the fraction of randomly oriented pairs of vectors with separation angle less than $\theta = 30°$ which are required to yield the corresponding average inner product on the left-hand abscissa. Top panel: the mean value of $\cos|\boldsymbol{L}\cdot\boldsymbol{L}(t_M)|$ for the full catalogue (solid line), LG catalogue (dotted line) and LG catalogue (dot-dashed line). Bottom panel: the mean value of $\cos|\boldsymbol{L}\cdot\boldsymbol{L}^{(1)}|$ for the full, SE and LG galaxy catalogues versus time.

5.6 Correlations

Our final examination of linear theory is to check whether equation (6) predicts the correct spin axis for a galaxy. Given the effects of the local tidal field examined in Section 5.2.2, it is possible that the direction of $\boldsymbol{L}$ will vary over time. In this case, since the direction of the predicted $\boldsymbol{L}^{(1)}$ remains fixed at its initial value, we find little reason to expect any long-term correlation between the two vectors. To test the stability of $\boldsymbol{L}(t)$, we plot the average value of the inner product of the angular momentum at turnaround $\boldsymbol{L}_M$ with $\boldsymbol{L}(t)$ for the full, LG and SE catalogues in Fig. 16 (top panel). Following turnaround, which occurs at roughly 2 Gyr, angular momentum is relatively stable in time, and hence the local tidal field predominantly affects only the magnitude rather than the direction.

To quantify the alignment of two vectors, we consider them weakly parallel if the angle between them is less than 30°. Table 7 lists the number of galaxies in each catalogue and the mass-scale for which the two vectors $\boldsymbol{L}$ and $\boldsymbol{L}^{(1)}$ are weakly parallel or antiparallel. We consider the vectors correlated if they satisfy the weakly parallel condition for at least 90 per cent of the epochs in the simulation. The probability of two randomly oriented vectors being separated by θ is given by the ratio of the arc subtended by θ to that of the unit circle $p = \theta/\pi$. For $\theta = 30°$, we expect 1/6 of randomly placed pairs of vectors to be aligned. The last column of Table 7 lists the number of correlated galaxies from each subset we expect if the orientation of $\boldsymbol{L}$ and $\boldsymbol{L}^{(1)}$ is completely random. In no case is the correlation more probable than random. To confirm this finding, we plot in Fig. 16 (bottom panel) the average absolute-value inner product of the two vectors for the full, LG and SE catalogues in time. For a randomly orientated distribution, $\langle\boldsymbol{L}\cdot\boldsymbol{L}^{(1)}\rangle = 2/\pi \simeq 0.64$, which we have marked in both panels. In the right-hand abscissa of each panel, we have indicated the fraction of randomly oriented pairs of vectors with separation angle less than $\theta = 30°$ which are required to yield the corresponding average inner product on the left-hand abscissa. We see that the alignment between the actual and predicted angular momentum does not occur more often than random from the above probability argument, and only occurs for roughly 10 per cent of the galaxies in the full catalogue, 18 per cent of the LG, and ~24 per cent of the SE catalogue. It thus appears that linear theory predicts the correct spin axis with, at most, only marginal statistical significance.

Table 7. Correlation statistics for $\boldsymbol{L}\|\boldsymbol{L}^{(1)}$.

	$M>$	N	$N_{\rm correlated}$	$N_{\rm anticorr.}$	$N_{\rm random}$
Full	0	77	5	4	12.8
	200	39	3	3	6.5
	1000	11	1	2	1.8
LG	0	52	4	4	8.7
	200	28	2	3	4.7
	1000	9	1	2	1.5
SE	0	34	4	4	5.7
	200	20	2	3	3.3
	1000	8	1	2	1.3

6 DISCUSSION AND CONCLUSIONS

In this paper we have examined the predictions of linear collapse and linear tidal-torque theory within the framework of a high-resolution N-body and hydrodynamical simulation. This permits the study of evolution well into the non-linear regime, thereby placing important constraints on the validity and applicability of linear theory to the full range of evolutionary periods. We have examined the evolution of dark matter, typical of galactic dark haloes.

The simplest treatment of galaxy evolution at early times follows the spherical-collapse model, in which we treat the protogalaxy as a spherically isotropic closed (i.e., overdense) distribution embedded within an Einstein–de Sitter universe. The

Downloaded from https://academic.oup.com/mnras/article-abstract/311/4/762/1746627 by California Institute of Technology user on 19 May 2020

observed evolution is qualitatively described by the ellipsoidal-collapse model (Peebles 1980; EL95) in which the short axis of the rotating ellipsoidal protogalaxy first collapses into a pancake, followed by collapse of the secondary and tertiary axes which form caustics that relax into virialized triaxial systems. While the spherical-collapse model greatly oversimplifies the observed collapse of galaxies (namely, it is a hierarchical and ellipsoidal process), analytic predictions correlate strongly with empirical measurements. The turnaround time t_M corresponds closely with the initial collapse of the short ellipsoidal axis. Furthermore, the epoch t_C at which this spherical model predicts shell crossings correlates closely with the collapse of the long axes of the evolving protogalaxy.

The linear-theory tidal-torque formalism (Section 2) predicts that the angular momentum L of a galaxy will grow linearly (equation 6) until turnaround, at which point self-gravitation dominates large-scale tidal torque. Since the quadrupole moment (on which the tidal field acts) of an elliptical ensemble remains significant until the long axis collapses, we synthesize a 'standard evolution' in which $L(t)$ grows linearly beyond turnaround, turns over during shell crossing, and remains constant as the galaxy relaxes and virializes. As *local* tidal interactions increase in strength and frequency, the evolution of L becomes increasingly noisy, but all our galaxies follow an underlying linear growth of L at early times. This agrees with analytic non-linear perturbative solutions of the Lagrangian fluid equations (Catelan & Theuns 1996b), which indicate that the initial torque on a galaxy is a good estimate of the torque during the entire period of angular-momentum acquisition, i.e., angular momentum will grow linearly in time since tidal torque is approximately constant. After shell crossing, the measured L appears to decrease, as a numerical result of the redistribution of angular momentum to bound particles outside the overdensity cut-off generated during galaxy identification. Unless all bound particles are identified in a galaxy (an N^2 calculation), the apparent decay of L at late times is a generic numerical trend of simulations.

We test the predicted total angular momentum, $L^{(1)}$, by comparing the value calculated from equation (6) to the true value of L at the turnaround, caustic crossing, and final epochs. Equation (6) at turnaround systematically overestimates the true turnaround $L(t_M)$ and the final L_f by a factor of $\sim$3, with a dispersion of roughly 70 per cent for lower mass galaxies, and 50 per cent for higher mass galaxies. This broad distribution of predicted versus actual angular momentum is expected from statistical analysis (HP88), and can be easily understood through, e.g., time-varying tidal effects, ellipsoidal collapse, and uncertainty in the actual epoch of decoupling of the galaxy from the large-scale tidal field. The nearly ubiquitous overestimation of L by linear theory observed in this and previous work is less easily explained. In the linear theory formalism, the angular momentum imparted to a galaxy equals the torque of a large-scale shear field on the moment arm of the initial particle distribution, which scales as the square of the distance. Furthermore, equation (6) explicitly assumes that the Taylor expansion of the potential ψ is constant both in time and throughout the collapsing volume at early times. If this approximation breaks down for outlying particles in the initial distribution (see Figs 1 and 2), the quadratic dependence of angular momentum with distance will inflate the predicted value $L^{(1)}$ (A. Heavens and R. Jimenez, private communication). This motivates a study of the inner mass-shells of collapsing galaxies, for which we expect that linear theory will more correctly model actual evolution.

The agreement of turnaround and final angular momenta implies that $L(t_M)$ is a robust estimator of L_f. However, given the result that angular momentum grows beyond turnaround due to ellipsoidal collapse, we suspect that if the decay of L post-shell crossing can be eliminated, then $L(t_C)$ at shell crossing will prove the more useful quantity. We find that the predicted direction of the angular momentum is only nominally more correlated with the true spin axis than we would expect from purely random alignment. Considering the rapid variation of local tidal fields due to neighbours and the non-linear redistribution of the inertial properties of an evolving galaxy, it is of little surprise that equation (6) only weakly predicts the direction of the angular momentum, and of even greater surprise that it does so closely predicts the magnitude. None the less, this underlines the limitations of applying linear theory to a highly non-linear problem.

Linear theory predicts that the final angular momentum varies proportionally to $M^{5/3}$ (equation 21), which we find to be robust from generalized least-squares fitting. Equations (6) and (21) further permit the calculation of ensemble averages and probability distributions without the need for lengthy numerical simulations. The predicted probability distribution of specific angular momentum versus mass (CT96), for example, matches closely with our data (Section 5.4). This tool may permit the numerical calculation of the angular-momentum function using the Press-Schechter formalism (Press & Schechter 1974), which estimates the mass function of collapsed objects in the universe. Theoretical correlations of shape, morphology, spin, and density will constrain models of galaxy formation once observations of dark-halo properties become available. It appears, however, that correlations involving the direction of the angular-momentum vector (such as the misalignment of $\boldsymbol{L}$ and the minor body axis) must be relegated to numerical simulations, since linear-theory predictions of the spin axes are statistically unreliable.

We examine trends in the initial density peaks of our galaxies, and compare them to predictions from the Gaussian-peaks formalism. Higher mass objects tend to originate from higher initial density peaks, with relatively few high-mass low-peak or low-mass high-peak objects. We question whether tidal torques not only spin up protogalaxies before turnaround, but also influence the volume of mass from which the galaxy evolves. Van de Weygaert & Babul (1994) find that the evolution of density peaks is highly sensitive to external shear, which can disrupt one peak into many haloes or form haloes from low-ν environments. EL95 determine from their study of elliptical collapse that the geometry of the collapsing region is determined largely by the external shear, and not uniquely by the initial high-density peak. Were there no significant tidal shear, anisotropies in the primordial medium would evolve roughly spheroidally, such that the final object would map surjectively to the initial density peak. However, local and large-scale tidal shear distorts the minor anisotropies in the high-density peak, resulting in a triaxial system which accretes mass from the surrounding lower density shells. The final bound object rarely resembles the initial region from which it evolved, and cannot be directly mapped back to the initial density peak. The spherical-collapse model is inadequate in this respect, since it cannot quantify the strong role of tidal shear on the collapse history.

From the spherical-collapse model, one expects that objects evolving from higher peaks collapse more quickly and spend less time in the linear regime. However, contrary to the corollary of this trend, galaxies from higher peaks also have higher final

Downloaded from https://academic.oup.com/mnras/article-abstract/311/4/762/1746627 by California Institute of Technology user on 19 May 2020

angular momenta. HP88 found this result for power spectra with fluctuations larger than the small-scale smoothing length. Since high peaks are statistically more correlated, they experience stronger tidal forces, and hence galaxies evolving from higher peaks are potentially subject to stronger local torque. These galaxies have shorter collapse times, since external tidal shearing tends to accelerate collapse and act as a source of internal gravity (Hoffman 1986; Zaroubi & Hoffman 1993; Bertschinger & Jain 1994; EL95). Perhaps more straightforward is the fact that, from the scaling correlation in equation (22), angular momentum scales significantly more strongly with mass than turnaround time. Although peak height and collapse time are inversely proportional, the direct variation of mass and peak height dominates, from which we expect that peak height and angular momentum will vary proportionally as well.

Our simulation evolved particles within only one-eighth of the comoving box. This significantly decreased the necessary CPU time while providing a realistic large-scale tidal field. However, galaxies evolving at the vacuum boundary of our subsampled region as well as those containing particles from the third, supermassive dark matter species had to be disregarded. Paper II will discuss this analysis within the framework of a full-scale, single-component simulation with 128^3 particles and identical initial conditions. This will provide at least eight times the number of bound objects, span a higher mass range, and will not suffer from conditions which force us to eliminate objects from our catalogue. Higher mass-scales will permit a study of internal mass shells, for which we expect that the consistent overprediction by linear theory of actual angular momentum will be resolved. It is uncertain how significantly the gas component effects the dynamics of dark-halo evolution; by comparing identical haloes in both simulations, we will also examine this question.

Numerous other statistical tests could be performed on our data set. Correlation functions of the principal axes and actual angular momentum of nearby neighbours (Splinter et al. 1997) can verify the underlying physics of the tidal-torque scenario, since the large-scale tidal field should cause nearest neighbours to spin about roughly the same axis, while the most distant neighbours should counter-rotate. BE87 test alignment statistics of axis vectors, angular-momentum and separation vectors between nearest neighbours to look also for coherence from tidal fields. The misalignment vector between the apparent spin axis and the projected short elliptical axis may indicate relationships between triaxial systems and ellipticities, and has been studied by, e.g., BE87, Frenk et al. 1988, Quinn & Zurek 1988, Franx et al. 1991, Dubinski 1992 and Warren et al. 1992. These tests rely on a larger statistical sample with larger dynamical resolution than we have available, and will thus be addressed in Paper II. We anticipate that the substantially larger data set will also reduce the uncertainty in the linear-theory prediction of angular momentum and permit more quantitative conclusions regarding peak-height correlations and scalings.

ACKNOWLEDGMENTS

BS thanks Jim Applegate for numerous enlightening discussions on celestial dynamics and mechanics, and Gino Thomas for his Socratic cynicism. Additional thanks to Raul Jimenez, Alan Heavens, Paolo Catelan and Tom Theuns for their interest, discussions and ideas, and to our referee, Joshua Barnes. This work was supported by the U.S. Department of Energy Outstanding Junior Investigator Award under contract DE-FG02-92ER40699, NASA grant NAG5-3091, the Alfred P. Sloan Foundation, Columbia Astrophysics Lab and the Columbia Department of Astronomy. This is contribution No. 676 from the Columbia Astrophysics Laboratory, and CU-TP-927 from the Columbia Physics Department.

REFERENCES

Bardeen J. M., Bond J. R., Kaiser N., Szalay A. S., 1986, ApJ, 304, 15
Barnes J., Efstathiou G., 1987, ApJ, 319, 575 (BE87)
Bertschinger E., Jain B., 1994, ApJ, 431, 486
Binney J., de Vaucouleurs G., 1981, MNRAS, 194, 679
Binney J., Silk J., 1979, MNRAS, 188, 273
Bond J. R., Efstathiou G., 1984, ApJ, 285, L45
Bond J. R., Meyers S. T., 1993, CITA, preprint 93/27
Bond J. R., Szalay A. S., 1983, ApJ, 274, 443
Catelan P., Theuns T., 1996a, MNRAS, 282, 436 (CT96)
Catelan P., Theuns T., 1996b, MNRAS, 282, 455
de Theije P. A. M., Katgert P., van Kampen E., 1995, MNRAS, 273, 30
Doroshkevich A. G., 1970, Afz, 6, 581
Dubinski J., 1992, ApJ, 401, 441
Dubinski J., 1994, ApJ, 431, 617
Dubinski J., Carlberg R. G., 1991, ApJ, 378, 496
Efstathiou G., Jones B. J. T., 1979, MNRAS, 186, 133
Efstathiou G., Silk J. I., 1983, Fundam. Cosmic Phys., 9, 1
Eisenstein D. J., Hut P., 1998, ApJ, 498, 137
Eisenstein D. J., Loeb A., 1995, ApJ, 439, 520 (EL95)
Evrard A. E., 1988, MNRAS, 235, 911
Fasano G., Vio R., 1991, MNRAS, 249, 629
Franx M., Illingworth G., de Zeeuw T., 1991, ApJ, 383, 112
Frenk C. S., White S. D. M., Davis M., Efstathiou G., 1988, ApJ, 327, 507
Gunn J. E., Gott J. R., 1972, ApJ, 176, 1
Heavens A. F., Peacock J. A., 1988, MNRAS, 232, 339 (HP88)
Hockney R. W., Eastwood J. W., 1981, Computer Simulation Using Particles. McGraw-Hill, New York
Hoffman Y., 1986, ApJ, 301, 65
Hoffman Y., 1988, ApJ, 329, 8
Hoyle F., 1949, in Burgers J. M., van de Hulst H. C., eds, Problems of Cosmical Aerodynamics, Central Air Documents. Dayton, Ohio, p. 195
Kaiser N., 1984, ApJ, 284, L9
Katz N., 1991, ApJ, 368, 325
Katz N., White S. D. M., 1993, ApJ, 412, 455
Kuhlman B., Melott A. L., Shandarin S. F., 1996, ApJ, 470, L41
Monaghan J. J., 1992, ARA&A, 30, 543
Ostriker J., 1993, ARA&A, 31, 689
Partridge R. B., Peebles P. J. E., 1967, ApJ, 147, 868
Peacock J. A., Heavens A. F., 1985, MNRAS, 217, 805
Peebles P. J. E., 1969, ApJ, 155, 393
Peebles P. J. E., 1971, A&A, 11, 377
Peebles P. J. E., 1980, The Large Scale Structure of the Universe. Princeton Univ. Press, Princeton, NJ
Peebles P. J. E., 1982, ApJ, 263, L1
Peebles P. J. E., 1993, Principles of Physical Cosmology. Princeton Univ. Press, Princeton, NJ
Plionis M., Barrow J. D., Frenk C. S., 1991, MNRAS, 249, 662
Politzer H. D., Wise M. B., 1984, ApJ, 285, L1
Press W. H., Schecter P., 1974, ApJ, 187, 425
Press W. H. et al., 1992, Numerical Recipes in Fortran, 2nd ed. Cambridge Univ. Press, Cambridge
Quinn T., Binney J., 1992, MNRAS, 255, 729
Quinn P. J., Zurek W. H., 1988, ApJ, 331, 1
Ryden B. S., 1988, ApJ, 329, 589
Ryden B. S., 1992, ApJ, 393, 445
Sciama D. W., 1955, MNRAS, 115, 3
Shandarin S. F., Zel'dovich Ya.B., 1989, Rev. Mod. Phys., 61, 185
Smoot G. F. et al., 1992, ApJ, 396, L1

Downloaded from https://academic.oup.com/mnras/article-abstract/311/4/762/1746627 by California Institute of Technology user on 19 May 2020

Splinter R. J., Melott A. L., Linn A. M., Buck C., Tinker J., 1997, ApJ, 479, 632
Statler T. S., 1987, ApJ, 321, 113
Summers F. J., 1993, PhD thesis, Univ. of California, Berkeley
Summers F. J., Davis M., Evrard A. E., 1995, ApJ, 454, 1
van de Weygaert R., Babul A., 1994, ApJ, 425, L59
Warren M. S., Quinn P. J., Salmon J. K., Zurek W. H., 1992, ApJ, 399, 405
White S. D. M., 1984, ApJ, 286, 38
White S. D. M., 1994, astro-ph/9410043
Zaroubi S., Hoffman Y., 1993, ApJ, 414, 20
Zaroubi S., Naim A., Hoffman Y., 1996, ApJ, 457, 50
Zel'dovich Ya. B., 1970, A&A, 5, 84

This paper has been typeset from a TEX/LATEX file prepared by the author.

Downloaded from https://academic.oup.com/mnras/article-abstract/311/4/762/1746627 by California Institute of Technology user on 19 May 2020